

Viscoelastic fluid flow in a 2D channel bounded above by a deformable finite thickness elastic wall

Debadi Chakraborty^{a,1}, J. Ravi Prakash^{a,*}

^aDepartment of Chemical Engineering, Monash University, Melbourne, VIC 3800, Australia

Abstract

The steady flow of three viscoelastic fluids (Oldroyd-B, FENE-P, and Owens model for blood) in a two-dimensional channel, partly bound by a deformable, finite thickness neo-Hookean solid, is computed. The limiting Weissenberg number beyond which computations fail to converge is found to increase with increasing dimensionless solid elasticity parameter Γ , following the trend Owens > FENE-P > Oldroyd-B. The highly shear thinning nature of Owens model leads to the elastic solid always collapsing into the channel, for the wide range of values of Γ considered here. In the case of the FENE-P and Oldroyd-B models, however, the fluid-solid interface can be either within the channel, or bulge outwards, depending on the value of Γ . This behaviour differs considerably from predictions of earlier models that treat the deformable solid as a zero-thickness membrane, in which case the membrane always lies within the channel. The capacity of the solid wall to support both pressure and shear stress, in contrast to the zero-thickness membrane that only responds to pressure, is responsible for the observed difference. Comparison of the stress and velocity fields in the channel for the three viscoelastic fluids, with the predictions for a Newtonian fluid, reveals that shear thinning rather than elasticity is the key source of the observed differences in behaviour.

Keywords:

2D channel flow, viscoelastic fluid, deformable finite-thickness neo-Hookean solid wall, fluid-structure interaction, microcirculation, finite element method

1. Introduction

Numerical simulation of blood transportation through the human cardiovascular system is an intense area of research [1–3]. Blood, which is rheologically complex, interacts with blood vessels walls both chemically and mechanically to give rise to an intricate fluid-structure interaction. From a fluid mechanics point of view, blood flow in large diameter blood vessels is commonly referred to as the macrocirculation, while flow in small vessels, such as arterioles, venules, and capillaries is referred to as the microcirculation. The Navier-Stokes equations are a good model for blood flow in the medium to large arteries, since Reynolds numbers are

*Corresponding author. Tel +61 3 9905 3274; Fax +61 3 9905 5686.

Email address: ravi.jagadeeshan@eng.monash.edu.au (J. Ravi Prakash)

¹Present address: Department of Mathematics and Statistics, The University of Melbourne, Victoria 3010, Australia

high, tube diameters are large, and blood can be considered to be an incompressible viscous Newtonian fluid. Most studies in the literature on fluid-structure interaction in the context of blood flow have so far been focused on the macrocirculation. In small vessels, however, where the shear rate is small, blood behaves as a non-Newtonian fluid due to its particulate nature. This necessitates its shear thinning, viscoelastic and thixotropic nature to be taken into account [4–7]. Another important aspect of the microcirculation is that the vessel wall thickness to diameter ratio is very high [8]. To the best of our knowledge, so far there have been no studies of fluid-structure interaction associated with the flow of viscoelastic fluids in vessels with finite thickness walls. The aim of this work is to examine the flow of a variety of viscoelastic fluid models interacting with a finite-thickness elastic vessel wall.

The study of fluid flow in collapsible channels and tubes has been motivated by the complex and nonlinear dynamics revealed by laboratory experiments [1, 9, 10]. The earliest and simplest theoretical models of collapsible-tube flow were lumped-parameter [11] and one dimensional models [12, 13], followed by two-dimensional models where part of one wall is replaced by a tensioned membrane in a two-dimensional rigid parallel sided channel. The membrane model assumes that the bending stiffness and extensibility of the wall in the flow direction can be ignored, and that the movement of the elastic wall is only in the direction normal to the wall. More recently, this basic model has been improved by using a plane strained elastic beam model for the collapsible wall with a Bernoulli-Euler beam, a Timoshenko beam and a 2D solid model [14–16]. Wall stiffness was found to play a major role in attaining a steady state solution, and for very small wall stiffness, the results of the beam model compared favourably with those of the membrane model. Work is ongoing on extending these models to describe 3D compliant tubes [16–21]. In all these studies, however, the fluid has always been treated as Newtonian. In this work, we examine the flow in a 2D collapsible channel of three different viscoelastic fluid models, namely, the Oldroyd-B, the FENE-P and the Owens model for blood [7], by considering the deformable wall to be a finite-thickness incompressible neo-Hookean solid. The channel dimensions are chosen to be compatible with the microcirculation.

The steady flow of Oldroyd-B, FENE-P and the Owens model fluids in a two-dimensional collapsible channel has been studied recently by Chakraborty et al. [22]. In contrast to the present work, however, the collapsible wall was modelled as a zero thickness membrane under constant tension [23]. It was shown that the predictions for the different viscoelastic fluids differ significantly from each other, with the key factor being the extent of shear thinning predicted by the individual models. In particular, it was shown that viscoelastic fluids behave identically to Newtonian fluids, provided that the viscosity of the two fluids at the location of the maximum shear rate in the channel is the same. Subsequently, Chakraborty and Prakash [24] examined the influence of the degree of shear thinning of the viscoelastic fluid by systematically varying the finite extensibility parameter b_M , in the FENE-P model, which controls the extent of shear thinning experienced by the fluid, and is consequently a convenient parameter for examining the influence of shear thinning. They found that the pressure drop, the molecular conformation tensor fields, and the stresses in the flow domain are significantly affected by the extent of shear thinning of the FENE-P fluid. Importantly, in both these studies, it was found that the significant differences that arise amongst the different

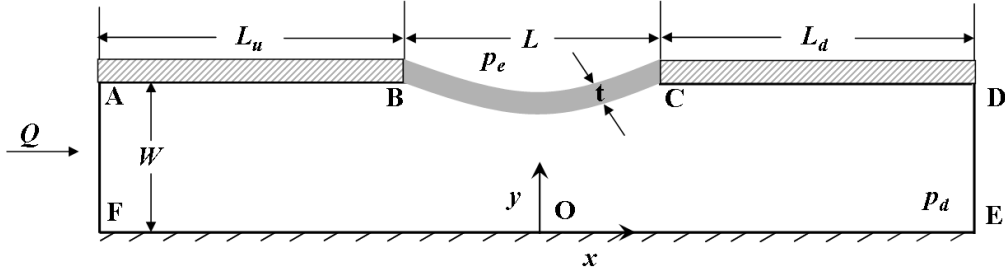


Figure 1: Geometry of the domain. $L_u = 7W$, $L = 5W$, and $L_d = 7W$. The wall thickness t is varied between $0.1W$ and $0.4W$.

viscoelastic fluids in the predicted value of the tangential shear stress on the membrane surface, has no influence on the shape of the deformable membrane, because of the boundary condition adopted in the work. Essentially it was assumed that the shape of the membrane is governed only by the normal stresses acting on it.

In order to use a more realistic model for the collapsible wall, Chakraborty et al. [25] replaced the zero thickness membrane with a finite thickness neo-Hookean solid, which can account for the effect of shear stress on the shape of the wall. The fluid was, however, assumed to be Newtonian. The model formulation followed the seminal work of Carvalho and Scriven [26], who examined roll cover deformation in roll coating flows, with the rubber roll cover modelled as either an incompressible neo-Hookean or a Mooney-Rivlin solid. Computational predictions of the deformation of the collapsible wall and pressure drop in the channel were found to be in good agreement with experimental measurements carried out in a polydimethylsiloxane microfluidic device, composed of a single microchannel with a thin flexible layer along one side of the channel.

The present work extends the model of Chakraborty et al. [25] by replacing the Newtonian fluid with Oldroyd-B, FENE-P and the Owens model viscoelastic fluids. The constitutive equations of all the viscoelastic fluids are written in conformation tensor form [27], and the fully coupled, steady state, fluid and solid equations are solved using the DEVSS-TG/SUPG (discrete elastic viscous stress split-traceless gradient) finite element method. Such a general formulation enables us to study the complex fluid-structure interaction that arises both from the capacity of the deformable wall to support shear and normal stresses, and from the shear thinning and viscoelastic nature of the fluid.

The plan of the paper is as follows. The problem formulation, with details of the governing equations for the viscoelastic fluids and incompressible neo-Hookean solid, the boundary conditions and the relevant dimensionless variables are presented in Section 2. The results of viscoelastic and Newtonian fluid computations are compared in Section 3. In particular, the dependence of the shape of the fluid-solid interface, and of the pressure, stress, conformation tensor and velocity fields on the different parameters, is examined. Finally, concluding remarks are drawn in Section 4.

2. Problem formulation

The geometry of the flow is that of a 2D channel, with one of the walls containing an elastic segment as illustrated in Fig. 1. In units of channel width W , the dimensions of the channel are $L_u = 7W$, $L = 5W$, and $L_d = 7W$. In most of the simulations, the solid wall has a thickness $t = 0.4W$.

2.1. Governing Equations

We have nondimensionalized the various physical quantities, by scaling lengths and displacements with W , velocities with GW/η_0 and pressure and stresses with G . Here G is the shear modulus of the solid, $\eta_0 (= \eta_s + \eta_{p,0})$ is the zero shear rate solution viscosity, η_s is the solvent viscosity and $\eta_{p,0}$ is the contribution of the microstructural elements to the zero shear rate viscosity. (For a Newtonian fluid, η_0 is just the constant Newtonian viscosity). Non-dimensionalization of the governing equations and boundary conditions yields the following dimensionless numbers:

$$Re = \frac{\rho W U_0}{\eta_0}; \quad \beta = \frac{\eta_s}{\eta_0}; \quad Wi = \frac{\lambda_0 U_0}{W}; \quad \Gamma = \frac{\eta_0 U_0}{GW}; \quad P = \frac{p}{G} \quad (1)$$

where Re is the Reynolds number, β is the viscosity ratio, Wi is the *inlet* Weissenberg number, Γ is the dimensionless solid elasticity parameter, P is the dimensionless pressure, ρ is the density of the liquid, U_0 is the average inlet velocity, λ_0 is the constant characteristic relaxation time of the microstructure. It is also convenient to define a *local* Weissenberg number $\widetilde{Wi} = \lambda_0 \dot{\gamma}$, which measures the non-dimensional shear rate at any location in the flow.

Upon introduction of these dimensionless variables, we can recast governing equations in the following dimensionless form:

$$\nabla \cdot \mathbf{v} = 0 \quad (\text{Mass balance}) \quad (2)$$

$$\frac{Re}{\Gamma} \mathbf{v} \cdot \nabla \mathbf{v} = \nabla \cdot \mathbf{T} \quad (\text{Momentum balance}) \quad (3)$$

$$\mathbf{v} \cdot \nabla \mathbf{M} - \nabla \mathbf{v}^T \cdot \mathbf{M} - \mathbf{M} \cdot \nabla \mathbf{v} = -\frac{\Gamma}{Wi} \{f(\text{tr } \mathbf{M}) \mathbf{M} - \mathbf{I}\} \quad (\text{Conformation tensor}) \quad (4)$$

$$\mathbf{T} = -P\mathbf{I} + \boldsymbol{\tau}^s + \boldsymbol{\tau}^p \quad (\text{Cauchy stress tensor}) \quad (5)$$

$$\boldsymbol{\tau}^s = \beta(\nabla \mathbf{v} + \nabla \mathbf{v}^T) \quad (\text{Viscous stress tensor}) \quad (6)$$

$$\boldsymbol{\tau}^p = (1 - \beta) \frac{\Gamma}{Wi} \{f(\text{tr } \mathbf{M}) \mathbf{M} - \mathbf{I}\} \quad (\text{Elastic stress tensor}) \quad (7)$$

$$\nabla_{\mathbf{X}} \cdot \mathbf{S} = 0 \quad (\text{Equation of motion for solid}) \quad (8)$$

$$\mathbf{S} = \mathbf{F}^{-1} \cdot \boldsymbol{\sigma} \quad (\text{First Piola-Kirchhoff stress tensor}) \quad (9)$$

$$\boldsymbol{\sigma} = -\pi\mathbf{I} + \mathbf{B} \quad (\text{Cauchy stress tensor for a neo-Hookean material}) \quad (10)$$

In these equations, \mathbf{v} is the velocity, ∇ denotes the gradient, \mathbf{I} is the identity tensor, π is the pressure, and \mathbf{B} is the left Cauchy-Green tensor, expressed as $\mathbf{B} = \mathbf{F} \cdot \mathbf{F}^T$. The deformation gradient tensor \mathbf{F} relates the undeformed state $[\mathbf{X} = (X, Y, Z)]$ to

the deformed state $\mathbf{x} = (x, y, z)$ and is expressed as:

$$\mathbf{F} = \frac{\partial \mathbf{x}}{\partial \mathbf{X}} \quad (11)$$

The form of $f(\text{tr } \mathbf{M})$ is model specific. For the Oldroyd-B model, $f(\text{tr } \mathbf{M}) = 1$, while for the FENE-P model [27],

$$f(\text{tr } \mathbf{M}) = \frac{b_{\mathbf{M}} - 1}{b_{\mathbf{M}} - \frac{\text{tr } \mathbf{M}}{3}} \quad (12)$$

where, $b_{\mathbf{M}}$ is the finite extensibility parameter, defined as the ratio of maximum length squared of the micro-structural element to its average length squared at equilibrium.

For the Owens model, $f(\text{tr } \mathbf{M}) = 1$ also holds, however, the *constant* relaxation time λ_0 in Eq. (4) is replaced by a *function* λ , which represents the relaxation time of the elastic stress due to blood cell aggregates. Note that this replacement is not carried out in Eq. (7), where the relaxation time remains constant and equal to λ_0 . The function λ depends on the average size of the blood cell aggregates, n , which is controlled by the competition of spontaneous aggregation and flow-induced disaggregation. Iolov et al. [28] have recently developed a finite element method for solving the Owens model in its complete generality. Since our focus here is on developing a fluid-structure interaction model that accounts for a viscoelastic fluid model and a finite thickness elastic wall, we assume for simplicity that the dynamics of n are fast with respect to other changes of the flow, i.e., $n = n_{\text{st}}(\dot{\gamma})$, which is its equilibrium value based on the local shear rate $\dot{\gamma} = \sqrt{2 \mathbf{D} : \mathbf{D}}$, where $\mathbf{D} = \frac{1}{2}(\nabla \mathbf{v} + \nabla \mathbf{v}^T)$ is the rate of strain tensor. This choice preserves the viscoelastic and shear thinning character of blood but does not capture its thixotropic behaviour [7]. This simplification makes it unnecessary to solve an additional equation for the variation of n in the flow domain. Under this assumption, the relaxation time λ is

$$\lambda = \left(\frac{\lambda_{\text{H}}}{\eta_{\text{p},\infty}} \right) \eta_{\text{p}}(\dot{\gamma}) \quad (13)$$

where, λ_{H} is the relaxation time of individual blood cell aggregates, $\eta_{\text{p},\infty}$ is the infinite shear-rate viscosity, and $\eta_{\text{p}}(\dot{\gamma})$ is their contribution to blood viscosity given by the Cross model,

$$\eta_{\text{p}}(\dot{\gamma}) = \eta_{\text{p},0} \left(\frac{1 + \theta_1 \dot{\gamma}^m}{1 + \theta_2 \dot{\gamma}^m} \right) \quad (14)$$

where m is a power law index, and the ratio of parameters θ_1 and θ_2 satisfies the expression, $\theta_1/\theta_2 = \eta_{\text{p},\infty}/\eta_{\text{p},0}$ [29]. More details on the current implementation of Owens model are given in Ref. [30]. The values of all model parameters used here are reported in section 3.2.

In free boundary flow problems, one of the major difficulties lies in the fact that the location of the free boundaries is unknown *a priori* and their solution is a part of the total solution. Here we use a boundary fitted finite element based elliptic mesh generation method [31–33] which involves solving the following elliptic differential

equation for the mapping:

$$\nabla \cdot \tilde{\mathbf{D}} \cdot \nabla \boldsymbol{\xi} = 0 \quad (15)$$

where $\boldsymbol{\xi}$ is a vector of positions in the computational domain and the dyadic, $\tilde{\mathbf{D}}$, is a function of $\boldsymbol{\xi}$, analogous to a diffusion coefficient, which controls the spacing of the coordinate lines [33].

As mentioned earlier, the formulation of the fluid-structure interaction problem posed here follows the procedure introduced previously by Carvalho and Scriven [26] in their examination of roll cover deformation in roll coating flows. However, it turns out that the weighted residual form of Eq. (8) used in their finite element formulation is incorrect. While the error does not lead to significant discrepancies for small deformations, it is serious for large deformations. The correct form of the weighted-residual equation is presented in Chakraborty et al. [25].

2.2. Boundary conditions and discretization

We prescribe the following boundary conditions:

1. No slip boundary conditions ($\mathbf{v} = \mathbf{0}$) are applied on the rigid walls.
2. Zero displacements are prescribed at the left side and right side of the solid.
3. At the upstream boundary, a fully developed dimensional velocity profile is specified in the form, $v_y = 0$ and $v_x = U_0 f(y/W)$ where U_0 is the average inlet velocity. In dimensionless form this can be represented as $v_x = \Gamma f(y/W)$ where, v_x is now non-dimensional. Since, for all the Wi considered here, the upstream velocity profiles for the Oldroyd-B and FENE-P fluids do not differ significantly from that of a Newtonian fluid, a Newtonian velocity profile is used. However, for the Owens model fluid, which is strongly shear thinning in nature, a different procedure is used. Since the viscosity of the Owens model fluid obeys power law scaling with shear rate at relatively low values of shear rate in simple shear flow (see section 3.1), we assume that the velocity profile at the upstream boundary is identical to the analytically computed velocity profile for a power-law fluid (with power law index m), flowing in a 2D channel. We find in our simulations (since the entrance length has been assumed to be sufficiently long), that the fully developed velocity profile of the Owens model fluid at the inlet to the collapsible channel is relatively unchanged from the analytical velocity profile imposed at the upstream boundary.
4. At the downstream boundary, the fully developed flow boundary condition is imposed, $\mathbf{n} \cdot \nabla \mathbf{v} = \mathbf{0}$ where \mathbf{n} is the unit normal to the outlet.
5. The conformation tensor equation for all the viscoelastic models is hyperbolic in nature and therefore boundary conditions are needed only on inflow boundaries. At the upstream inflow, the conformation tensor does not change along the streamlines because the flow is fully developed [34, 35]. Thus,

$$\mathbf{v} \cdot \nabla \mathbf{M} = 0 \quad (16)$$

6. A force balance and a no-penetration condition are prescribed at the interface between the liquid and solid domain.

$$\mathbf{n} \cdot \mathbf{T} = \mathbf{n} \cdot \boldsymbol{\sigma} \quad \text{and} \quad \mathbf{v}_{solid} = \mathbf{v}_{fluid} \quad (17)$$

where \mathbf{n} is the unit normal to the deformed solid surface.

7. A force balance is prescribed at the top surface.

$$\mathbf{n} \cdot \boldsymbol{\sigma} = -P_e \mathbf{n} \quad (18)$$

where P_e is the dimensionless external pressure.

8. The non-dimensional pressure of the fluid at the downstream boundary, P_d , is set equal to zero.

Equations (2), (3), (4) and (15) are converted into a set of algebraic equations by the DEVSS-TG finite element method [34, 36], which introduces the traceless interpolated velocity gradient \mathbf{L} [34]

$$\mathbf{L} - \nabla \mathbf{v} + \frac{1}{\text{tr} \mathbf{I}} (\nabla \cdot \mathbf{v}) \mathbf{I} = 0 \quad (19)$$

In the transport equations the rate of strain tensor \mathbf{D} is calculated from the interpolated velocity gradient \mathbf{L} .

The weighted residual form of Eqs. (2), (3), (4), (8), (15) and (19), yields a large set of coupled non-linear algebraic equations, which is solved by Newton's method with analytical Jacobian, frontal solver, and first order arclength continuation in parameters [22, 34, 37, 38]. Note that while Eqs. (2), (3), (4), (15) and (19) are implemented in the fluid domain, Eq. (8) is solved in the solid domain.

3. Results and discussions

A thorough validation of the finite-element code, in the context of a Newtonian fluid, has been carried out by Chakraborty et al. [25], who have compared results obtained with the present formulation with several earlier results obtained in different contexts.

It is appropriate to briefly discuss the fluid models used in the present work before presenting the results of our simulations, since the differences in behaviour amongst them is essentially due to differences in their rheology.

3.1. Fluid models and choice of parameters

Each of the three fluids examined here has distinct qualitative features: (i) The Oldroyd-B fluid is viscoelastic, but does not shear thin. Furthermore, its uniaxial extensional viscosity is unbounded. (ii) The FENE-P fluid is viscoelastic, shear thins, and has a bounded uniaxial extensional viscosity. (iii) The Owens model fluid is viscoelastic and shear thins, but has an unbounded uniaxial extensional viscosity. Additionally, a notable feature of the Owens model, which belongs to the class of White-Metzner fluids, is that the dependence of viscosity η_p on shear rate $\dot{\gamma}$ can be prescribed arbitrarily through the choice of parameters in the Cross model (see Eq. (14)). In particular, the viscosity can be prescribed independently of the relaxation time. In contrast, for the FENE-P model, the dependence of η_p on the shear rate $\dot{\gamma}$ is completely determined by the choice of the parameters, $\eta_{p,0}$, λ_0 , and the finite extensibility parameter b_M . Unlike in the case of the Owens model, no further control can be exerted on the shape of the viscosity function.

The difference in the prediction of viscosity by the FENE-P and Owens models, as a function of the Weissenberg number $\widetilde{Wi} = \lambda_0 \dot{\gamma}$, in steady shear flow, is displayed

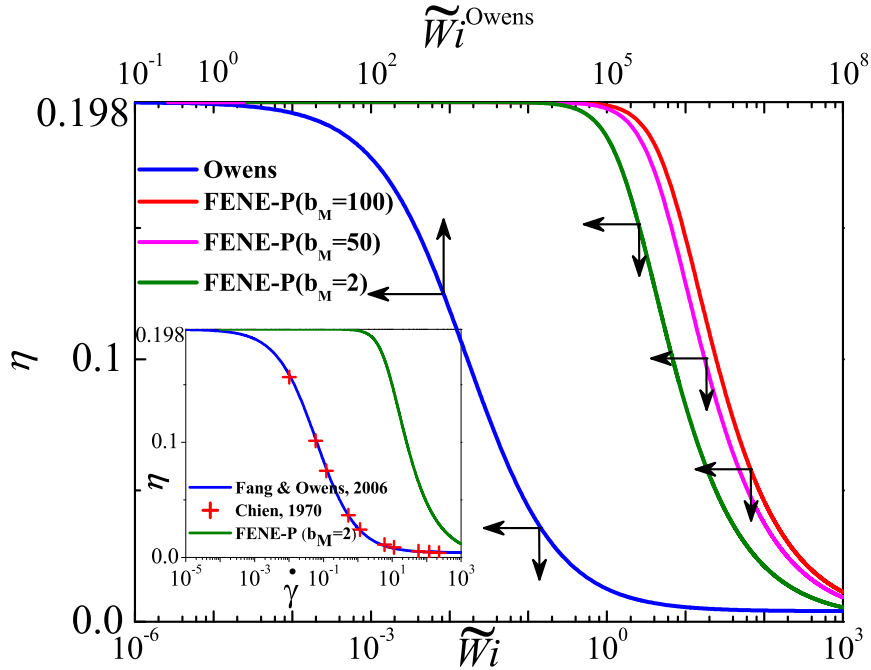


Figure 2: The contribution of the microstructure to the total viscosity, η , for the Owens model and FENE-P fluids in steady shear flow as a function of Weissenberg number \widetilde{Wi} . The inset shows the shear rate dependence of viscosity in the Owens model, fitted to the experimental results for blood reported by Chien [39], and the predictions of the FENE-P model for $b_M = 2$ and $\lambda_0 = 0.263$.

in figure 2. For the Owens model, we set $\eta_{p,0} = 0.197$ Pa s, $\eta_{p,\infty} = 0.003$ Pa s, $\eta_s = 0.001$ Pa s, $\theta_2 = 8$, and $m = 0.75$. These parameter values were chosen by Fang and Owens [29] to fit experimental data for the steady-state viscosity of blood, as reported by Chien [39]. The fitted curve and experimental data are reproduced in the inset to figure 2. Additionally, Fang and Owens [29] suggest $\lambda_H = 0.004$ s, which leads to $\lambda_0 = 0.263$. In order to compare the two fluid models, we assume that the FENE-P model has the same value of $\eta_{p,0}$ and λ_0 , and that η_s is the same. This assumption is based on the expectation that any choice of viscoelastic model would have to be compatible with known experimental information on the rheology of the fluid, which would, at the least, include a knowledge of the zero shear rate viscosity and the relaxation time. Note that for the FENE-P model, while there is no necessity to prescribe λ_0 when the shear rate dependence of viscosity is expressed in terms of Wi , it is necessary when represented in terms of $\dot{\gamma}$. As is well known, the FENE-P model predicts increasing shear thinning with decreasing values of the finite extensibility parameter b_M . The entire family of curves for the FENE-P model shown in figure 2, with values of b_M ranging from 100 to 2, does not shear thin as rapidly as the Owens model. In particular, it is clear from the inset that for the parameters recommended by Fang and Owens [29], the FENE-P model is unable to capture the rapidity with which blood shear thins, even for

$b_M = 2$. In all cases, in line with expectation, shear thinning first occurs for the FENE-P fluid when $\widetilde{Wi} \sim O(1)$. For viscoelastic fluids, the onset of shear thinning at $\widetilde{Wi} \sim O(1)$ implies that for shear rates $\dot{\gamma} > 1/\lambda_0$, the fluid no longer responds in a Newtonian manner, and that the longest time scale for micro-structural relaxation is comparable to λ_0 . Since the Owens model shear thins at $\widetilde{Wi} \ll 1$, this suggests that the characteristic time scale for micro-structural rearrangement is much larger than λ_0 . As mentioned earlier, λ_0 corresponds to the relaxation time for an aggregate of blood cells, which according to Owens [7], are typically of a size that represents the greatest proportion of erythrocytes. By defining a Weissenberg number $\widetilde{Wi}^{\text{Owens}}$ for which the Owens model fluid shear thins when it is of $O(1)$ (see the upper horizontal axis of figure 2), we can estimate that the appropriate relaxation time is of order 10^4 , which must correspond to much larger structures than a typical blood cell aggregate. We do not explore this aspect further here, rather, for the purposes of the present paper, we assume that the FENE-P and Owens models are distinct constitutive models, which have the same zero shear rate material properties, but shear thin significantly differently. As will be discussed in greater detail in the sections below, the difference between the models leads to significant differences in their behaviour.

For all the computational results reported here, we set $\eta_{p,0}$, $\eta_{p,\infty}$, η_s , θ_2 , and m at the values recommended by Fang and Owens [29]. However, we vary λ_0 (by varying λ_H) in order to control the inlet Weissenberg number. For the FENE-P fluid, we set $b_M = 100$, which is a value commonly used in simulations. As we are interested in small blood vessels, we choose the width W of the channel to be $100 \mu\text{m}$ and $U_0 = 0.01 \text{ m/s}$, inline with the data reported in Robertson et al. [40]. The value of Re in small blood vessels is well below 1. We have not seen any significant difference in the profile shape of the collapsible wall for values of Re in the range of 0-1, so we set $Re = 0$ by setting $\rho = 0$.

Deng and Guidoin [41] and Intengan et al. [42] have reported the values of Young's modulus (E) for the human artery to be in the range 200-4000 kPa. Zhang and co-workers [43–46] have reported the Young's modulus of the porcine artery to be in the range 110-140 kPa, while using two different values for the external pressure (8 kPa and 9.3 kPa) in their experimental measurements of the Young's modulus. In order to adequately represent the microcirculation, we choose a wide range of values for the external pressure p_e from 1.2 to 16 kPa and G (which is equal to $E/3$) in the range 30 to 400 kPa. Since $P_e = p_e/G$, we keep P_e fixed at a constant value of 0.04 even though both p_e and G are varied. On the other hand, we vary Γ in the range 4.95×10^{-5} to 6.6×10^{-4} . For most of the simulations reported here, a fixed value of $0.4W$ is chosen for the thickness of the solid wall (t), as the artery wall thickness to vessel diameter ratio is typically very high in small blood vessels [8]. However, in section 3.4, a few results of simulations with varying wall thickness are discussed to elucidate the effect of wall thickness.

3.2. Mesh convergence and the high Weissenberg number problem

Chakraborty et al. [22] have established that the flow in a collapsible channel with a zero-thickness membrane suffers from the high Weissenberg number problem and have shown that there is a limiting Weissenberg number for each of the fluid models beyond which computations fail. Furthermore, this limiting Wi value

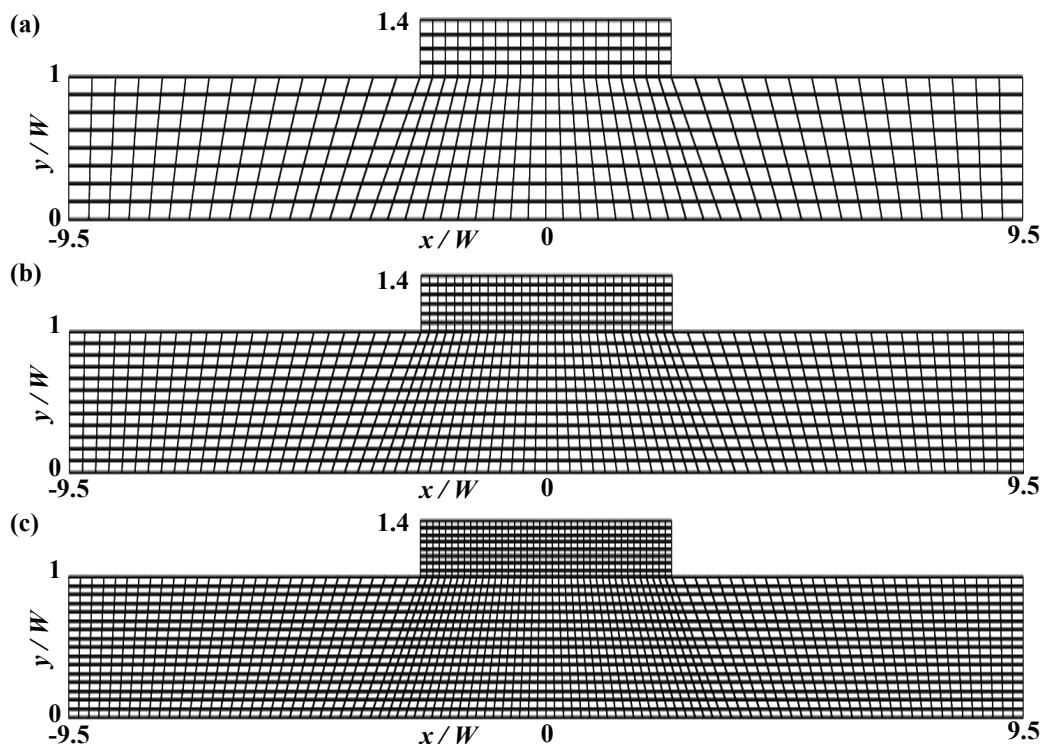


Figure 3: Meshes considered in the current study. (a) M1, (b) M2, and (c) M3, for $t = 0.4W$.

Mesh	Number of elements	Number of nodes	Degrees of freedom
M1	400	1705	10972
M2	900	3757	24072
M3	1600	6609	42252

Table 1: Meshes considered in the current study.

has been shown to increase with mesh refinement. Here we study mesh convergence over a range of parameters for the current geometry, using three different meshes M1-M3 for $t = 0.4W$, as illustrated in figure 3, with the mesh details given in Table 1.

In viscoelastic flow, mesh convergence is generally studied by examining the values of the invariants of the conformation dyadic, \mathbf{M} . The eigenvalues m_i of the conformation dyadic represent the square stretch ratios along the principal directions of stretching m_i for an ensemble of molecules [27, 34]. It has been well established that the breakdown of viscoelastic computations is typically due to the smallest eigenvalue becoming negative in some regions of the flow domain [22, 34, 38, 47, 48].

Figure 4 shows the maximum eigenvalue m_3 and minimum eigenvalue m_1 of the conformation tensor as a function of Wi for the Oldroyd-B, FENE-P and Owens fluids at $\Gamma = 4.95 \times 10^{-5}$ and $P_e = 0.04$ for $t = 0.4W$. Figures 4 (a)-(c) clearly exhibit the breakdown of viscoelastic computations at a particular value of Weissenberg

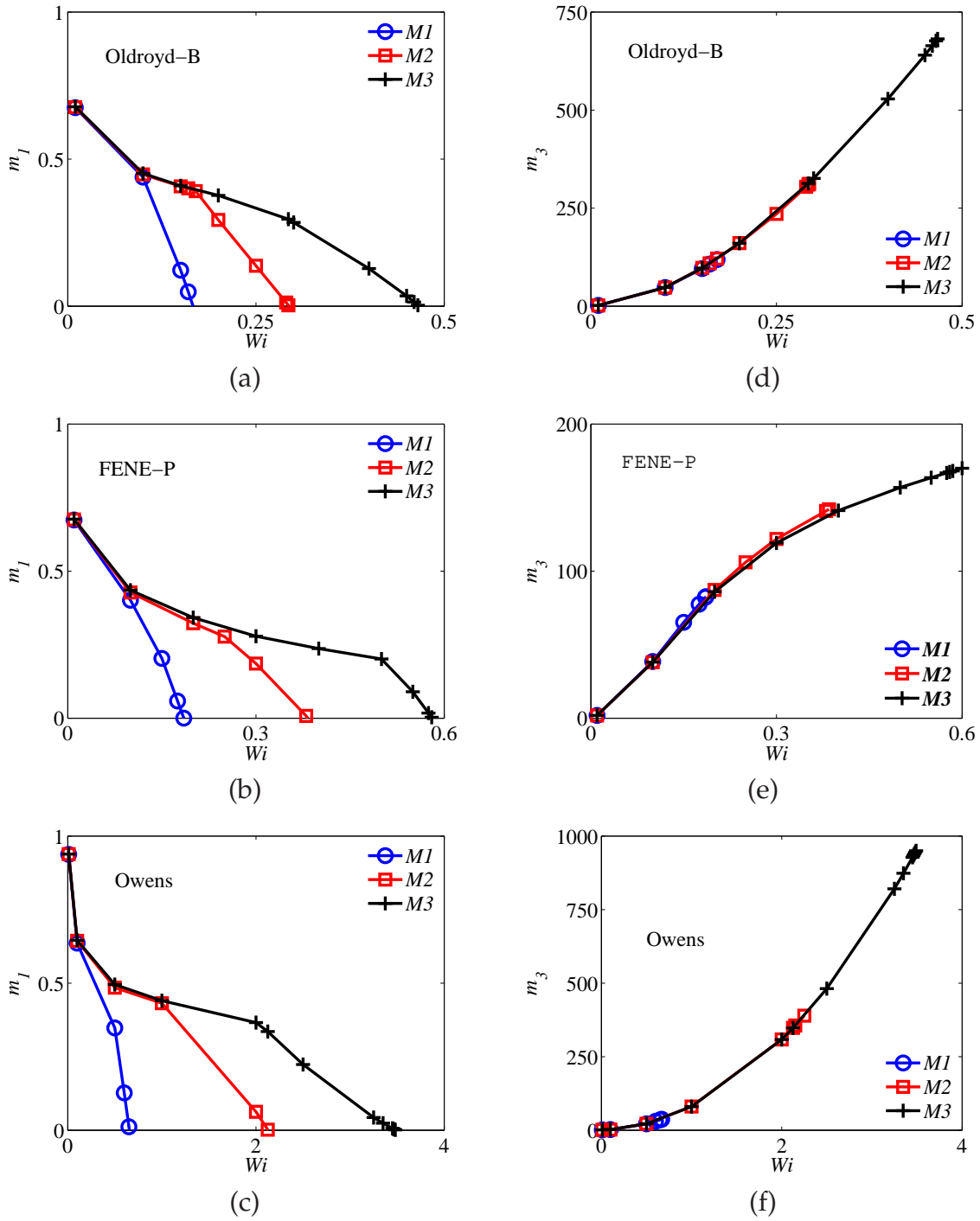


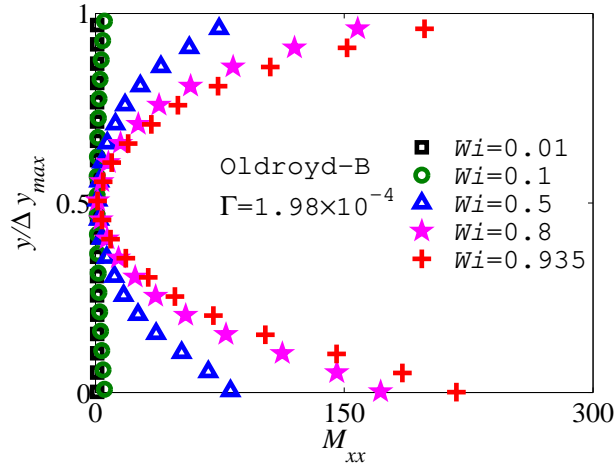
Figure 4: Minimum value of the smallest eigenvalue (m_1) and maximum value of the largest eigenvalue (m_3) in the entire flow domain, for the Oldroyd-B ((a) and (d)), FENE-P ((b) and (e)), and Owens model ((c) and (f)), as a function of Wi at $\Gamma = 4.95 \times 10^{-5}$ and $P_e = 0.04$ for $t = 0.4W$.

number on each mesh, since the minimum value of m_1 becomes negative. This limiting Wi increases with increase in mesh refinement.

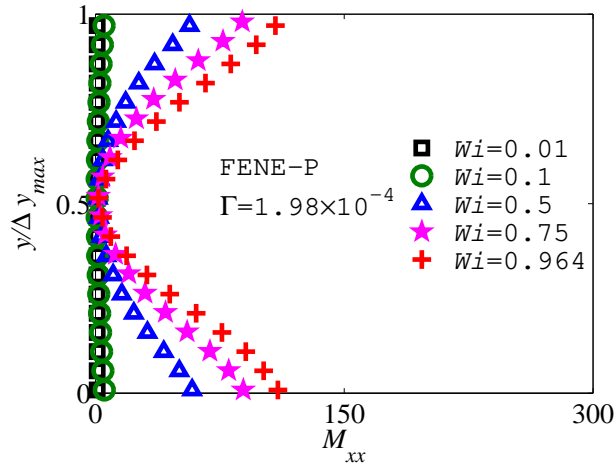
An increase in Wi leads to a higher maximum m_3 and lower minimum m_1 across the flow domain. While the breakdown value of Wi at each mesh can be anticipated from the sudden change of the slope of the curves in the minimum m_1 plots (figure 4 (a)-(c)), the curves of the maximum m_3 on various meshes overlap with each other (figures 4 (d)-(f)). The limiting value of Wi on the M2 mesh for the Oldroyd-B, FENE-P and Owens fluids is respectively 0.29, 0.38 and 2.13, while the mesh converged value of Wi for these models is 0.17, 0.20 and 1.0 respectively. In all our analysis, we have ensured that mesh converged values of Wi are used for any particular mesh.

While figure 4 displays the maximum and minimum eigenvalues in the entire flow field, figure 5 displays the mean streamwise molecular stretch M_{xx} across the channel at the point where the gap between the flexible and rigid walls is a minimum, for a fixed value of Γ , and increasing values of Wi . With increasing Weissenberg number, M_{xx} grows nearly symmetrically from a relatively low value in the middle of the gap, to a significantly larger value near the bottom (rigid) and top (flexible) walls. Note that in the Oldroyd-B and Owens models, M_{xx} is unbounded due to the infinite extensibility of the Hookean spring in the Hookean dumbbell model which underlies these fluid models. Conversely, the existence of an upper bound to the mean stretchability of the spring in the FENE-P model restricts the maximum value for M_{xx} , which for $b_M = 100$ is 300. The profiles of M_{xx} for the different fluids in figure 5 clearly reflect this micro-mechanical aspect of the models, and confirm that as in other benchmark problems for non-Newtonian flow, numerical computations in a 2-D collapsible channel also fail due to the development of large stresses and stress gradients in certain regions of the flow field, which are related to large changes in the conformations of the molecules.

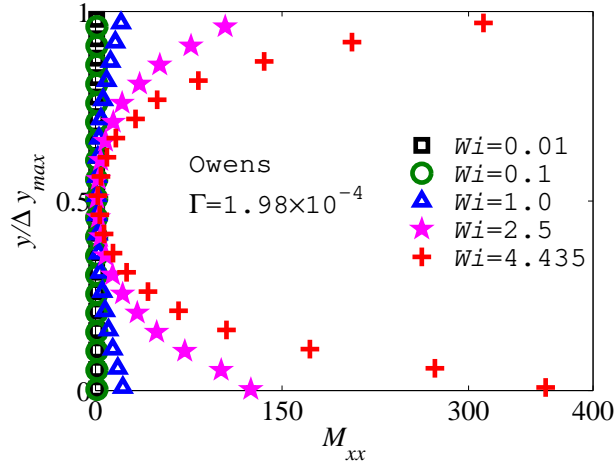
In their earlier study with a zero-thickness membrane, Chakraborty et al. [22] have shown that the extent of collapse of the membrane also has a significant effect on the limiting Weissenberg number. As the gap in the channel becomes narrower with decreasing tension in the membrane, the fluid is 'squeezed' leading to a greater deformation of the molecules, with a concomitant numerical breakdown at smaller values of Wi . One of the parameters that controls the deformability of the wall in the current work is Γ (the other being wall thickness t , whose influence on the limiting Wi is discussed subsequently in section 3.4). Figure 6 displays the limiting and the mesh converged values of the Weissenberg number for the M2 mesh, as a function of Γ . The limiting Weissenberg number follows the trend Owens > FENE-P > Oldroyd-B. For the Oldroyd-B and FENE-P models, the limiting and mesh converged Weissenberg numbers appear to increase with an increase in Γ for values of $\Gamma \lesssim 4.0 \times 10^{-4}$, before levelling off at higher values of Γ . On the other hand, for the Owens model fluid, $Wi_{Limiting}$ and $Wi_{Converged}$ increase monotonically with Γ . The Owens model fluid also exhibits the biggest difference between the converged and limiting values of Wi . As will be apparent when we discuss the shape of the fluid solid interface in figure 7, an increase in Γ leads to an increase in the magnitude of the narrowest channel gap, and consequently an increase in the limiting value of Wi .



(a)



(b)



(c)

Figure 5: Profile of M_{xx} across the narrowest channel gap for the Oldroyd-B, FENE-P and Owens models, for a range of Weissenberg numbers, at $\Gamma = 1.98 \times 10^{-4}$, $P_e = 0.04$ and $t = 0.4W$. For the FENE-P fluid, we set $b_M = 100$. The distance from the bottom channel is scaled by the narrowest gap width Δy_{max} (see figure 8(a) for a definition) of the particular model.

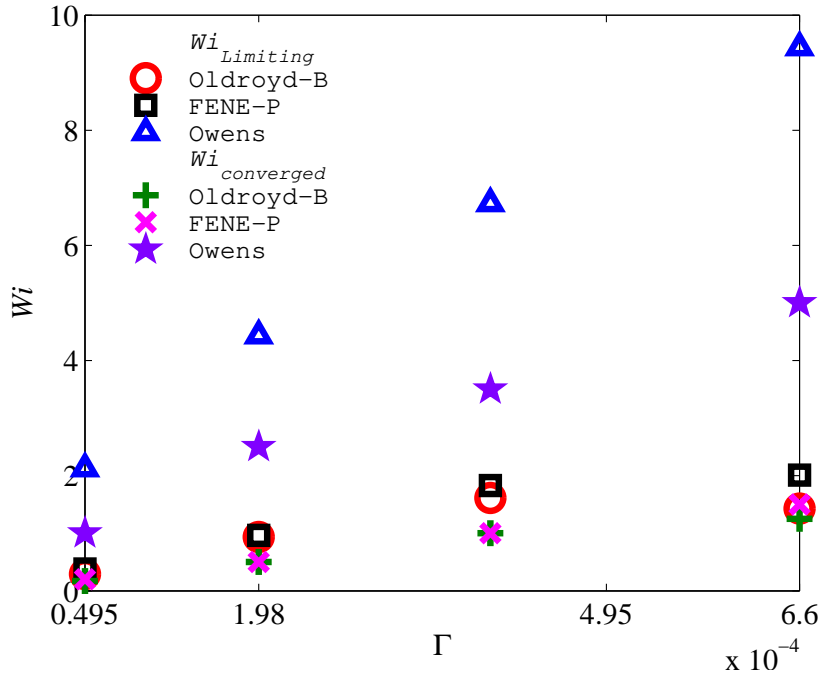


Figure 6: Maximum mesh converged value of Wi and the limiting Wi , for the three fluid models, for computations carried out with the M2 mesh, at $Pe = 0.04$ and $t = 0.4W$, as a function of Γ .

3.3. Interface shape and velocity contours

Figure 7 explores the deformation of the finite-thickness solid wall, while interacting with the different fluids, at a fixed value of $t = 0.4W$. While figures 7 (a)-(c) investigate the shape of the fluid-solid interface for different values of Γ at $Wi = 0.1$, figures 7 (d)-(f) examine the dependence of the interface profile on Wi for $\Gamma = 4.95 \times 10^{-4}$. The extraordinary variation in the shape of the elastic solid with varying elasticity parameter Γ is immediately apparent from figures 7 (a)-(c). In particular, there is a stark contrast in the response of the solid to the flow of different viscoelastic fluids. Except in the case of the Owens model, increasing Γ leads to a movement of the deformable solid from being within the channel (concave downwards) to bulging out of the channel (convex upwards) due to action of the forces exerted by the flowing fluid. At the relatively low value of $Wi = 0.1$ there is no discernible difference between the Newtonian, Oldroyd-B and FENE-P fluids. For the Owens model on the other hand, while the elastic solid remains concave downwards for the entire range of Γ values, there is a decrease in the minimum channel gap with increasing Γ . This behaviour is related to the significant difference in the force field generated in the Owens model fluid due to flow, as discussed shortly.

It is appropriate to note here that in our earlier investigation of viscoelastic flow in a 2D channel with a zero-thickness membrane [22], the fluid-solid interface was always observed to be concave downwards for all the viscoelastic fluids, at all values of membrane tension. Indeed, in contrast to the situation for a finite thickness solid, with decreasing tension, the zero-thickness membrane moves further into the channel, with a concomitant decrease in the narrowest channel gap.

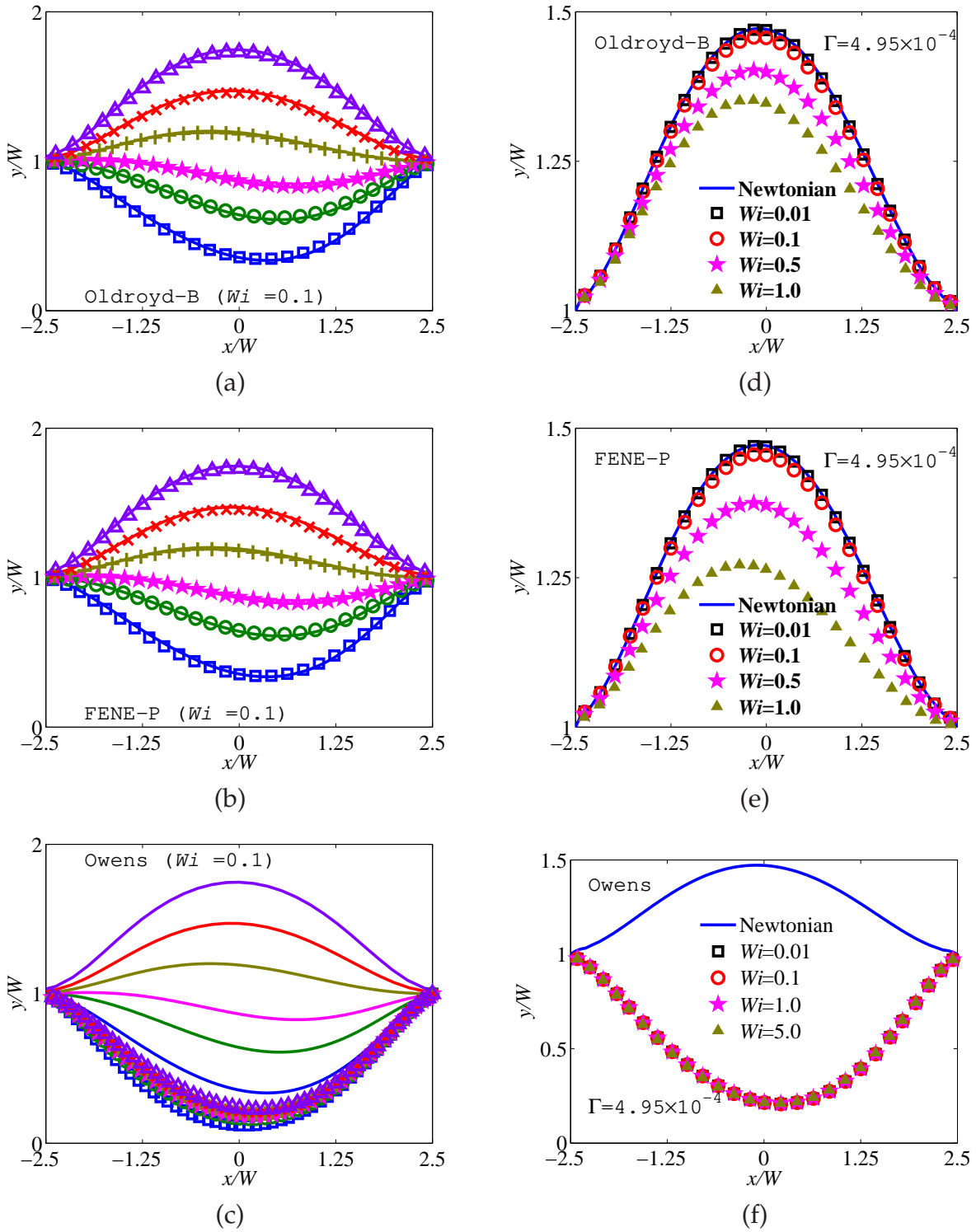
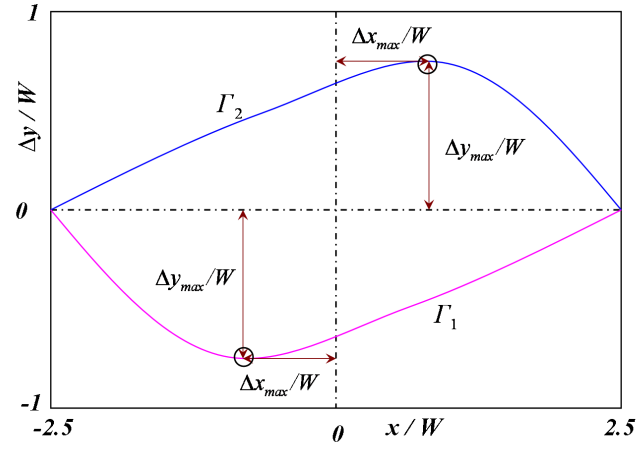
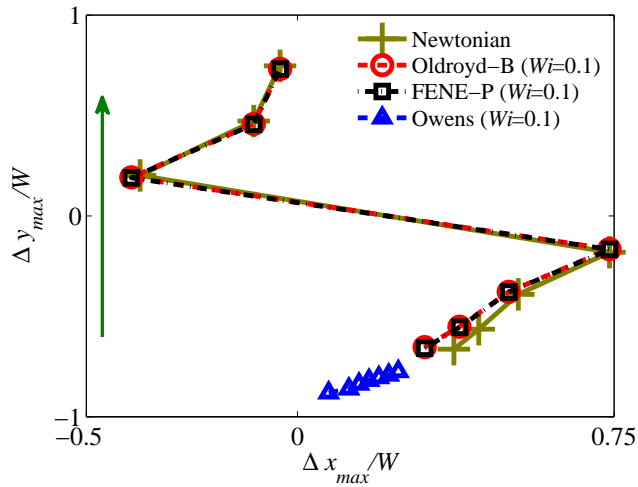


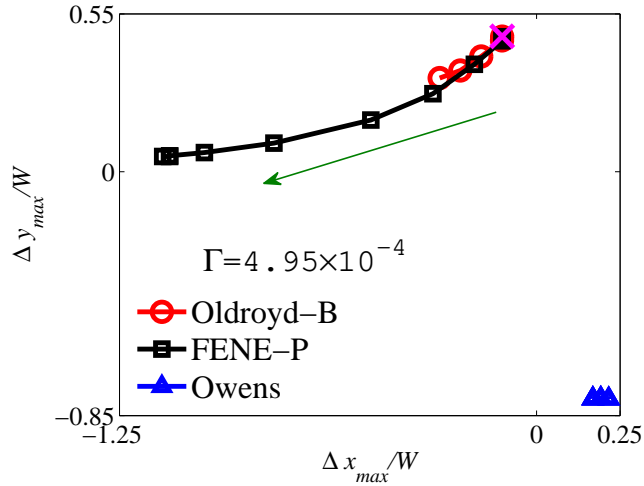
Figure 7: The shape of the fluid-solid interface in a 2-D collapsible channel for the Oldroyd-B ((a) and (d)), FENE-P ((b) and (e)) and Owens models ((c) and (f)), compared with the profile for a Newtonian fluid. Note that Wi is 0.1 in (a)–(c) and Γ is 4.95×10^{-4} in (d)–(f). In (a)–(c) different symbols represent different values of Γ (\square : 4.95×10^{-5} , \circ : 1.98×10^{-4} , \star : 3.0×10^{-4} , $+$: 3.96×10^{-4} , \times : 4.95×10^{-4} and \triangle : 6.6×10^{-4}). Lines with the same colour as the symbols represent the predictions of a Newtonian fluid for identical values of Γ .



(a)



(b)



(c)

Figure 8: (a) Schematic diagram defining the position of maximum deformation ($\Delta x_{max}, \Delta y_{max}$). (b) Dependence of $(\Delta x_{max}, \Delta y_{max})$ on Γ at a fixed value of $Wi = 0.1$, and (c) on Wi at a fixed value of $\Gamma = 4.95 \times 10^{-4}$. In (b) and (c) the arrows indicate the direction of increasing Γ and Wi , respectively. The range of Wi for the Oldroyd-B, FENE-P and Owens models are 0.01-1.508, 0.01-2.372 and 0.01-7.9, respectively.

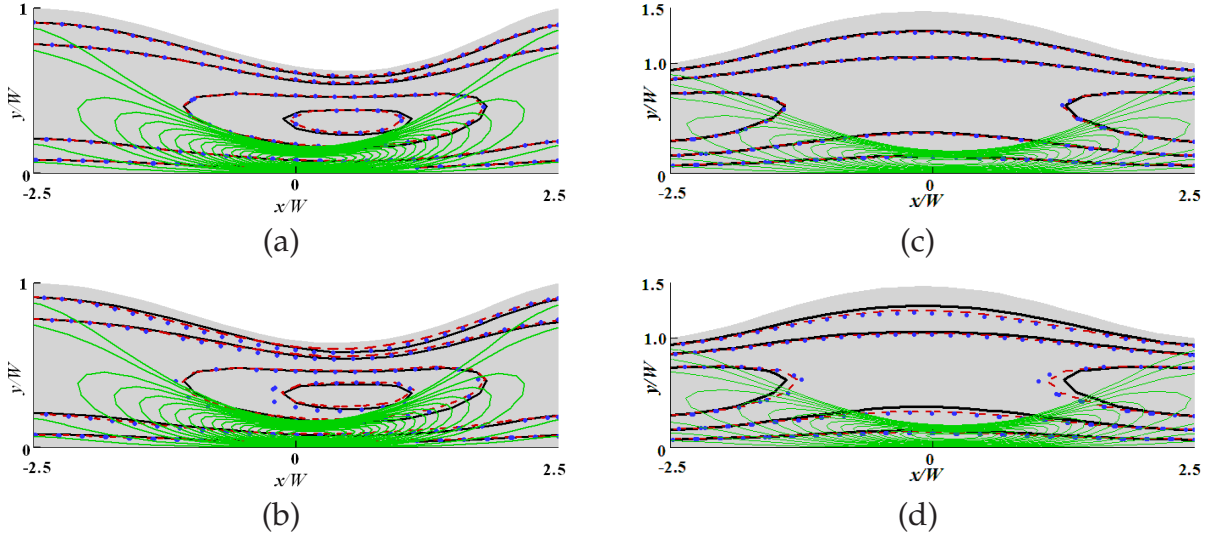


Figure 9: Contours of axial velocity (v_x) in the flow domain, for Newtonian (black), Oldroyd-B (red), FENE-P (blue) and Owens (green) fluids at $P_e = 0.04$, $t = 0.4W$, for two different values of Weissenberg number $Wi = 0.1$ ((a) and (c)) and $Wi = 0.5$ ((b) and (d)). Note that $\Gamma = 1.98 \times 10^{-4}$ in (a)-(b) and $\Gamma = 4.95 \times 10^{-4}$ in (c)-(d). The upper boundary in these figures reflects the shape of the interface at the corresponding parameter values.

At a fixed value of elasticity parameter Γ , while figure 7 (f) indicates that Wi has no effect on the shape of the deformable solid in the case of the Owens model (which remains concave downwards), it has a noticeably different effect for the Oldroyd-B and FENE-P fluids. Both fluids cause the elastic solid to bulge outwards. However, the extent of this bulge decreases more rapidly for the FENE-P fluid with increasing Wi . In the case of the Owens model, at these values of Wi , shear thinning is nearly complete, and there is consequently no change discernible in the membrane shape. On the other hand, the onset of shear thinning for the FENE-P model is responsible for the observed variation in the predicted membrane shape from that for an Oldroyd-B fluid.

Figure 7 indicates that the deformation of the solid wall occurs along both axial and vertical directions for all the fluid models, with the extent of movement depending on the values of Γ and Wi . By defining the position of maximum deformation as the point on the elastic solid furthest in the vertical direction from the horizontal surface, this dependence can be examined more systematically. The precise location of the position of maximum deformation is given by the co-ordinate pair $(\Delta x_{max}, \Delta y_{max})$, as shown schematically in figure 8 (a), which measures the maximum displacement from the centre of the elastic solid when it is horizontal. Figures 8 (b) and 8 (c) track the position of maximum deformation for varying Γ and Wi , and correspond to the set of figures 7 (a) to (c) and 7 (d) to (f), respectively. The movement of the elastic solid from being concave downwards to convex upwards in the case of varying Γ , and the downward movement with increasing Wi are clearly captured in this description. The relative immobility of the solid in the case of a flowing Owens model fluid is also clearly revealed.

Figure 9 compares the velocity contours predicted by a Newtonian fluid with those of an Oldroyd-B, FENE-P and Owens' fluid at $P_e = 0.04$ and $t = 0.4W$, for

two different values of Γ and Wi . The qualitative and nearly quantitative similarity of the velocity contours for the Oldroyd-B and FENE-P models with those for a Newtonian fluid at $Wi = 0.1$ and $Wi = 0.5$ suggests that fluid rheology does not have a significant influence on the velocity field at these values of Wi . On the other hand, the dominant influence appears to be the value of the elasticity parameter Γ , which determines the shape of the fluid-solid interface. While the velocity contours for all the fluids are qualitatively similar to each other when the elastic solid lies within the channel (figures 9 (a) and (b) for the Oldroyd-B and FENE-P models, and figures 9 (a) to (d) for the Owens model), there is a qualitative change when the elastic solid lies outside the channel. The latter situation occurs only for the Oldroyd-B and FENE-P models for $\Gamma = 4.95 \times 10^{-4}$, as displayed in figures 9 (c) and (d).

3.4. Influence of wall thickness on interface shape and limiting Weissenberg number

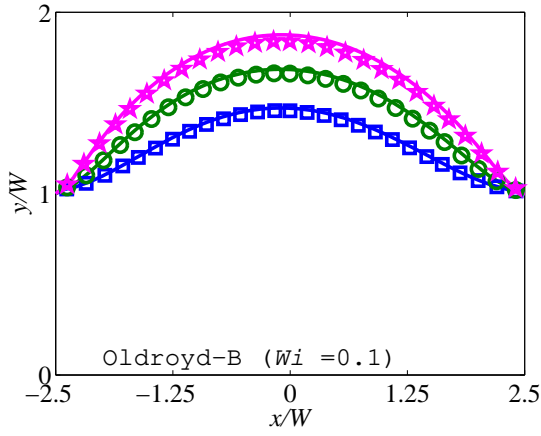
The wall thickness t does not appear directly in the governing equations, or in the boundary conditions, rather it determines the size of the solid domain. We can anticipate, however, that its influence on the interface shape and limiting Weissenberg number will be similar to that of the elasticity parameter Γ . In very simple terms, increasing Γ for a given state of stress at the fluid-solid interface due to the flow of viscoelastic fluid in the channel, leads to a larger strain in the solid, since (with all other parameter values fixed) an increase in Γ implies a decrease in the shear modulus of the solid, G . Similarly, for a given state of stress at the fluid-solid interface, decreasing the wall thickness t would lead to a larger strain in the solid, since there is “less” solid material over which to distribute the resultant stress in the solid.

These arguments are borne out in figures 10, which explores the deformation of the finite-thickness solid wall, while interacting with the different fluids, at a fixed value of $\Gamma = 4.95 \times 10^{-4}$. While figures 10 (a)-(c) investigate the shape of the fluid-solid interface for different values of t at $Wi = 0.1$, figures 10 (d)-(f) examine the dependence of the interface profile on Wi for $t = 0.1W$.

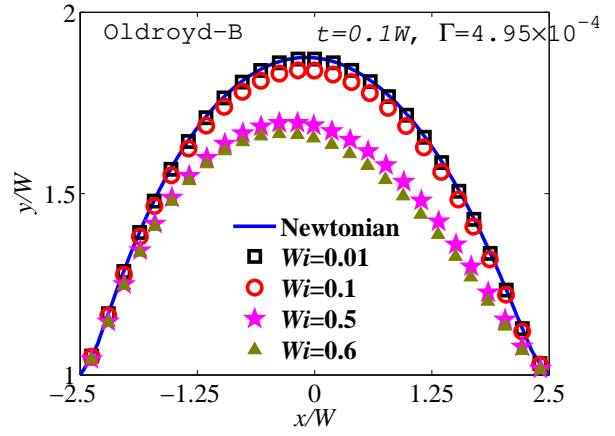
Figures 10 (a) and (b) indicate that for $\Gamma = 4.95 \times 10^{-4}$, at all values of t examined here, the solid wall bulges outward, and there is no discernible difference between the Oldroyd-B and FENE-P models, and a Newtonian fluid. For all these fluids, increasing t leads to a decrease in the extent of deformation of the solid wall. The profiles are similar to those observed previously in figures 7 (a) and (b) for decreasing values of Γ . In the case of the Owens model fluid, the fluid-solid interface lies within the channel for all the examined values of wall thickness. However, there is a distinct change observed in the shape of the interface, with the profile becoming more symmetric as the value of t increases.

The change in interface shape with increasing Wi , at fixed values of t and Γ , displayed in figures 10 (d)-(f) is very similar to that observed previously in figures 7 (d)-(f), with the extent of shear thinning playing the dominant role in determining the shape. The essential difference between the two sets of figures appears to be in the loss of symmetry in the interface profile for the smaller value of t .

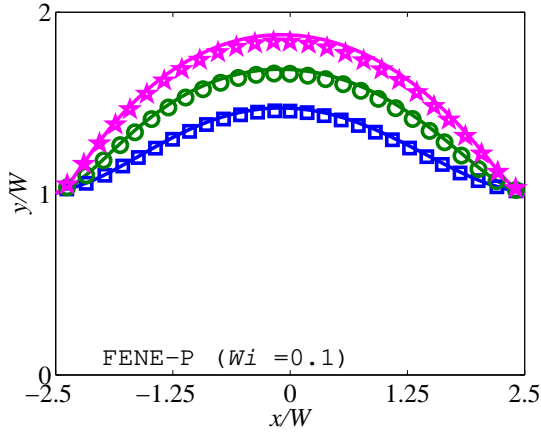
As discussed earlier, both the mesh converged and limiting Weissenberg numbers for the Owens model increase with increasing Γ because of an increase in the narrowest channel gap (see figures 6 and figure 7 (c)). This argument is consistent



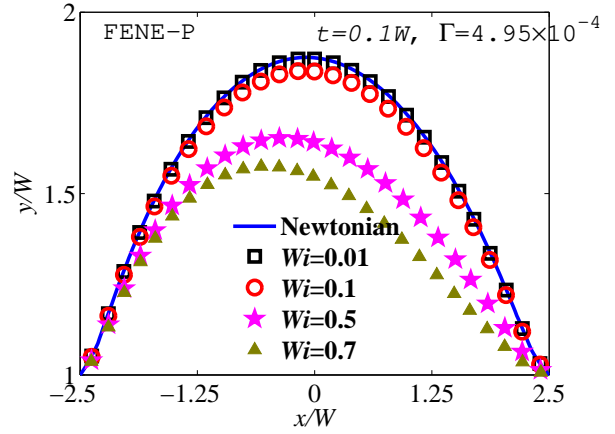
(a)



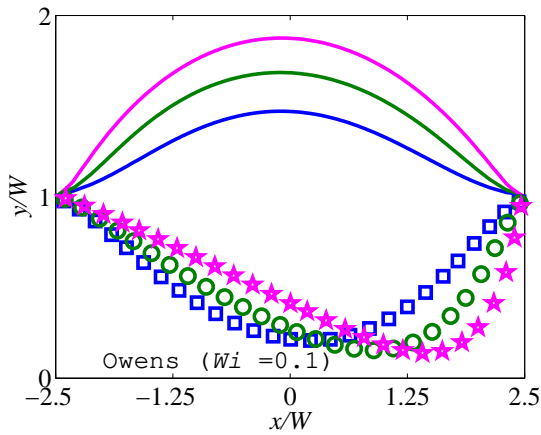
(d)



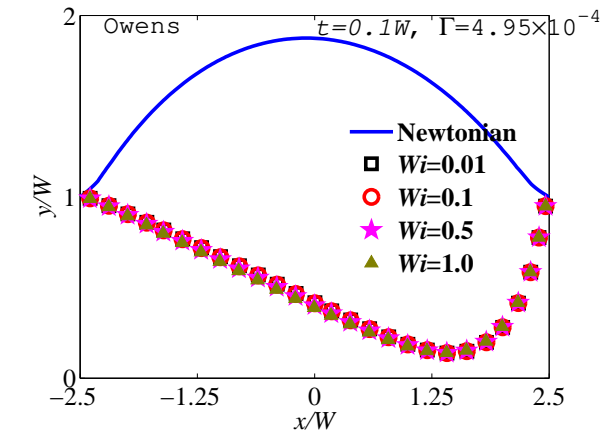
(b)



(e)



(c)



(f)

Figure 10: The shape of the fluid-solid interface for the Oldroyd-B ((a) and (d)), FENE-P ((b) and (e)) and the Owens model fluids ((c) and (f)), compared with the profile for a Newtonian fluid, at different values of wall thickness t and Wi , at a fixed value of $\Gamma = 4.95 \times 10^{-4}$. The value of Wi is fixed at 0.1 in (a)–(c), while t is fixed at $0.1W$ in (d)–(f). In (a)–(c) different symbols represent different values of t (\star : $0.1W$, \circ : $0.2W$, \square : $0.4W$). Lines with the same colour as the symbols represent the predictions of a Newtonian fluid for identical values of t .

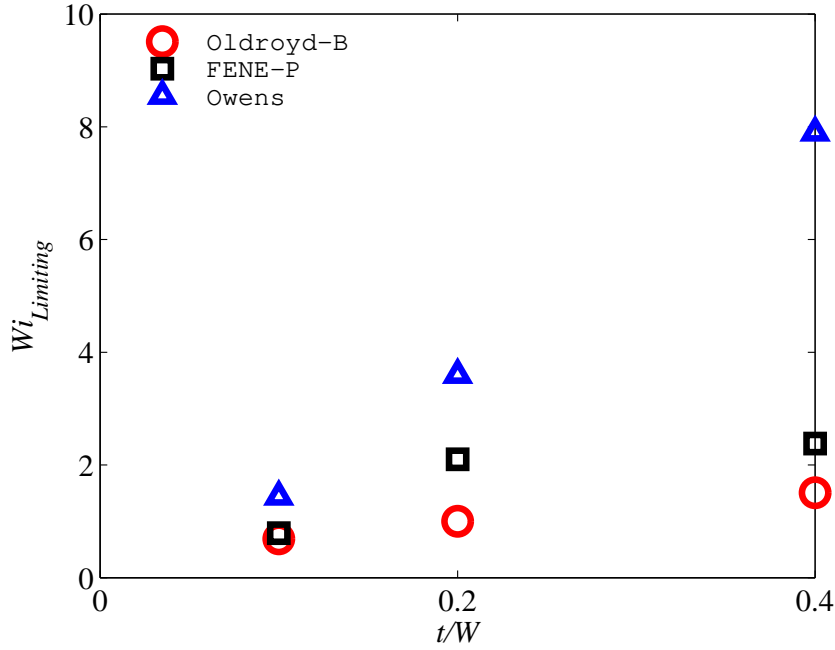


Figure 11: Limiting Weissenberg number for the three fluid models, for computations carried out with the M2 mesh, at $P_e = 0.04$ and $\Gamma = 4.95 \times 10^{-4}$, as a function of the non-dimensional wall thickness t/W .

with the behaviour of $Wi_{Limiting}$ displayed in figure 11 for the Owens model, for increasing values of t/W (see also figure 10 (c)). In both these situations corresponding to the Owens model, the elastic wall always lies within the channel for all the values of the various parameters considered here. We have seen previously in figure 6, for both the Oldroyd-B and FENE-P models, that $Wi_{Limiting}$ and $Wi_{Converged}$ are not sensitive to changes in Γ for values of Γ that correspond to the situation where the elastic wall lies outside the channel. On the other hand, figure 11 suggests that even though the elastic wall lies outside the channel for $\Gamma = 4.95 \times 10^{-4}$ (see figures 10(a) and (b)), $Wi_{Limiting}$ increases with t/W , until $t/W = 0.2$, before levelling off.

3.5. Pressure and stresses

Patankar et al. [49] have shown analytically that for any constitutive model of the form,

$$a_1 \mathbf{D} + a_2 \overset{\vee}{\mathbf{D}} + a_3 \mathbf{T} + a_4 \overset{\vee}{\mathbf{T}} = \mathbf{0} \quad (20)$$

where, a_1 , a_2 , a_3 , and a_4 are scalar functions of the invariants of \mathbf{D} and \mathbf{T} , and $\overset{\vee}{\mathbf{D}}$ and $\overset{\vee}{\mathbf{T}}$ are the upper convected time derivatives of \mathbf{D} and \mathbf{T} , the *normal component* of extra stress on a rigid body surface will be zero. Chakraborty et al. [22] have shown numerically that this is true even in the case of flow past a deformable zero-thickness membrane, for all the three viscoelastic fluids considered here. In the present instance as well, we find that the normal component of stress on the elastic wall is solely due to pressure.

Figure 12 examines the effect of Γ and Wi on the non-dimensional pressure P

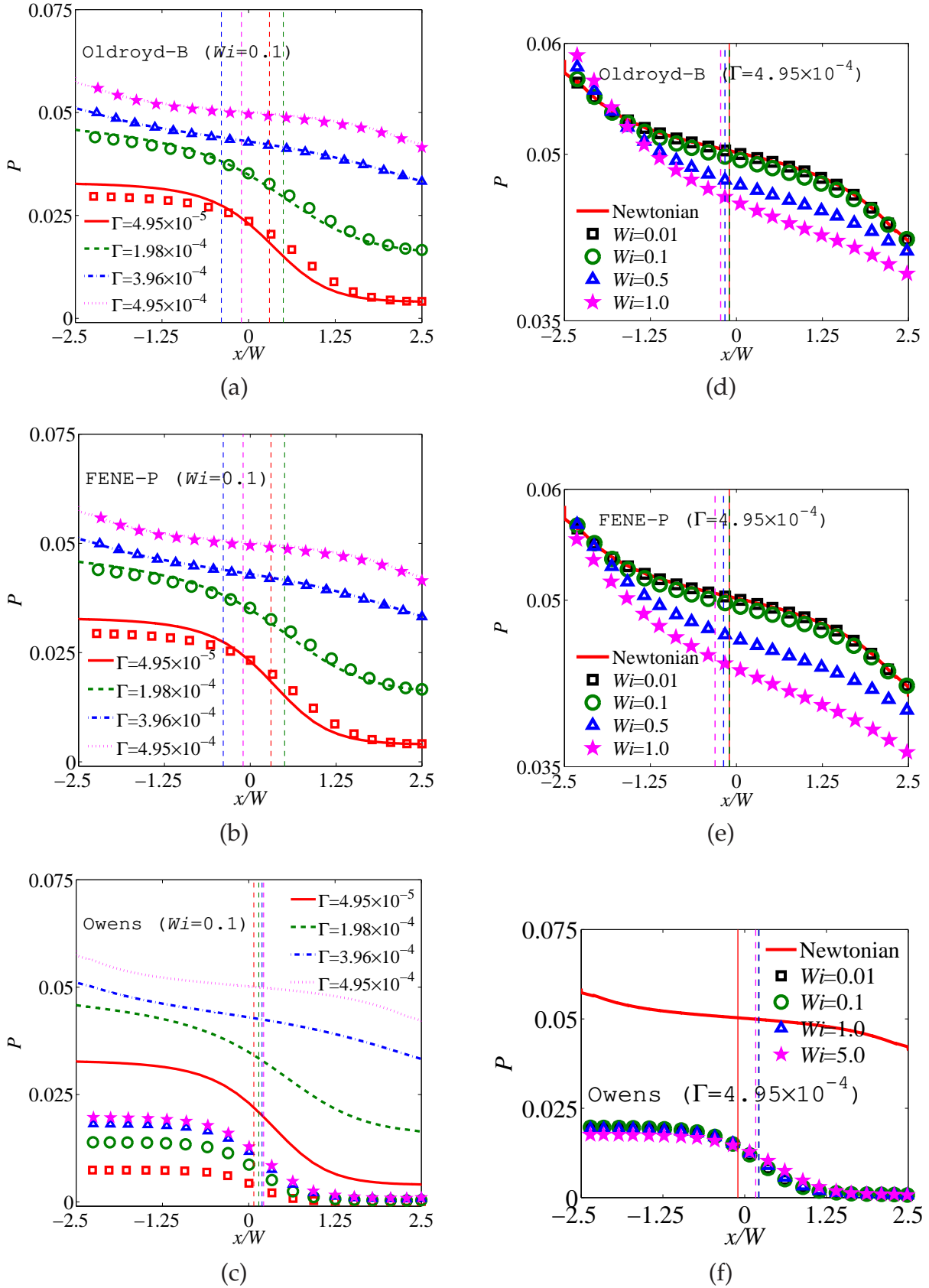


Figure 12: Dependence of the pressure profile along the flexible membrane on Wi and Γ , for the Oldroyd-B ((a) and (d)), FENE-P ((b) and (e)) and Owens models ((c) and (f)), respectively. The lines in (a)–(c) are for a Newtonian fluid. Note that $\Gamma = 1.98 \times 10^{-4}$ in (d)–(f) and $Wi = 0.1$ in (a)–(c).

exerted by the different fluids on the elastic solid. At $Wi = 0.1$, the increase in P with increasing Γ for the Oldroyd-B and FENE-P models is nearly identical to that for a Newtonian fluid, as can be seen from figures 12 (a) and (b). Notably, for all these fluids, a distinct change occurs in the shape of the pressure profile for $\Gamma > 1.98 \times 10^{-4}$. For values of Γ less than or equal to this value, the pressure profile is relatively constant upstream of the position of maximum deformation, before decreasing relatively rapidly downstream to a constant value. (The vertical lines in the figure denote the x -position of maximum deformation, with the colour coordinated to match the corresponding Γ value). On the other hand, for values of $\Gamma > 1.98 \times 10^{-4}$, the decrease in pressure from the location where the fluid flows under the deformable solid to the location where it exits, is much more uniform. As can be seen from figures 7 (a) and (b), the change in the shape of the pressure profile is correlated with the change in interface shape that occurs around $\Gamma \sim 3 \times 10^{-4}$, which is approximately the value at which the elastic solid moves from being concave downwards within the channel to bulging outwards from the channel. In the case of the Owens model, even though the pressure increases with increasing Γ , the shape of the pressure profile remains unchanged, since the elastic solid is always concave downwards in shape (see figures 12 (c) and 7 (c)). Another notable aspect is that the magnitude of pressure at any point along the interface is significantly lower for the Owens model compared to that for all the other fluids. This can be attributed to the significant decrease in viscosity that occurs for the Owens model fluid when it flows under the deformable solid.

Figure 12 (d)-(e) display the effect of Wi on the pressure profile for a fixed value of $\Gamma = 4.95 \times 10^{-4}$. At this value of Γ , as seen earlier in figures 7 (d)-(f), for all the values of Wi considered here, the elastic solid bulges outwards from the channel due to interaction with the Oldroyd-B and FENE-P fluids, while it is concave downwards for the flow of an Owens model fluid. In the former two cases, with increasing Wi , there is a clear decrease in the pressure that the fluid exerts on the downstream end of the elastic solid, with the decrease being more substantial for the FENE-P fluid. This correlates with the decrease in the bulge of the elastic solid seen earlier in figures 7 (d) and (e). For the Oldroyd-B fluid, there also appears to be a slight increase in pressure at the upstream end of the elastic solid. In the case of the Owens model fluid, neither the interface shape nor the pressure profile are significantly altered by the variation in Wi .

Figures 13 display the pressure contours under the collapsible wall for all the fluids at $P_e = 0.04$ and $t = 0.4W$, for different values of Γ and Wi . As was observed earlier in the case of velocity contours in figures 9, the qualitative shape of the pressure contour depends strongly on whether the elastic solid lies within or outside the channel. Thus, shapes for all the fluids are similar to each other in figures 13 (a) and (b), while the shapes for the Newtonian, Oldroyd-B and FENE-P fluids differ qualitatively from that of Owens model fluid in figures 13 (c) and (d), since the elastic wall lies inside the channel in the latter case while lying outside for the former.

The pressure contours for the Oldroyd-B and FENE-P fluids are quantitatively similar to those for the Newtonian fluid only for the case when $Wi = 0.1$ and $\Gamma = 1.98 \times 10^{-4}$ (figure 13 (a)). On the other hand, they depart from the Newtonian contours at the remaining values of Wi and Γ displayed in figures 13 (b) to (d). This is consistent with the behaviour of the pressure profiles along the fluid-solid

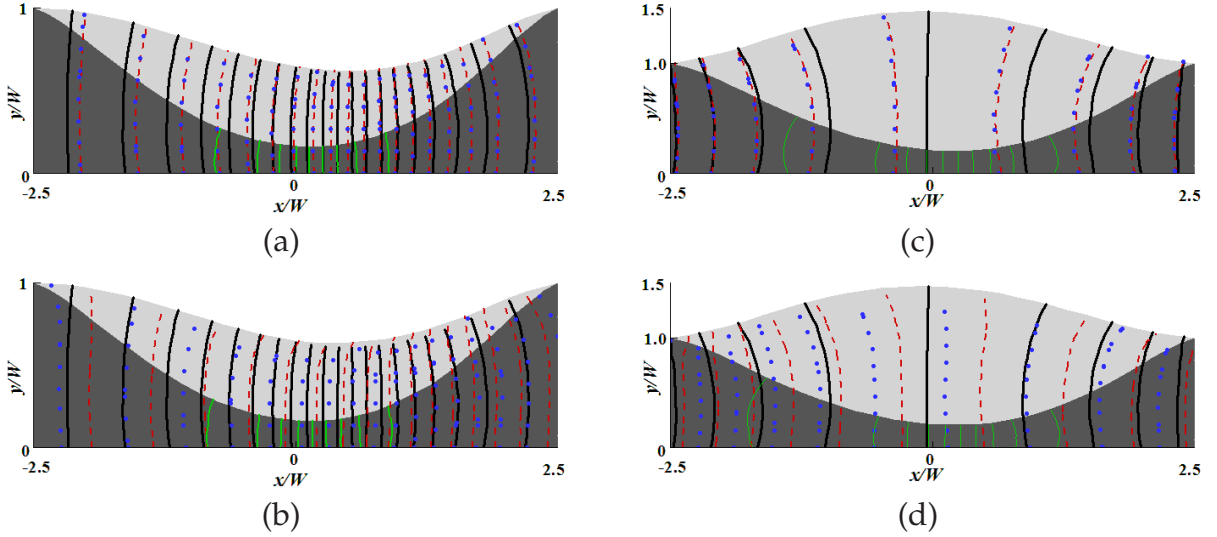


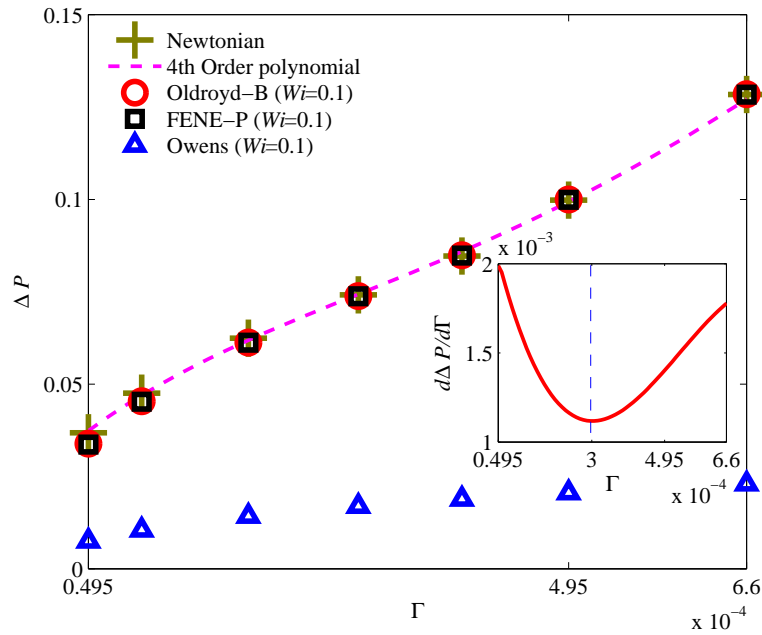
Figure 13: Contours of pressure in the flow domain, for Newtonian (black), Oldroyd-B (red), FENE-P (blue) and Owens (green) fluids at $P_e = 0.04$, $t = 0.4W$ for two different values of Weissenberg number $Wi = 0.1$ ((a) and (c)) and $Wi = 0.5$ ((b) and (d)). Note that $\Gamma = 1.98 \times 10^{-4}$ in (a)-(b) and $\Gamma = 4.95 \times 10^{-4}$ in (c)-(d).

interface observed in figures 12 (a), (b), (d) and (e).

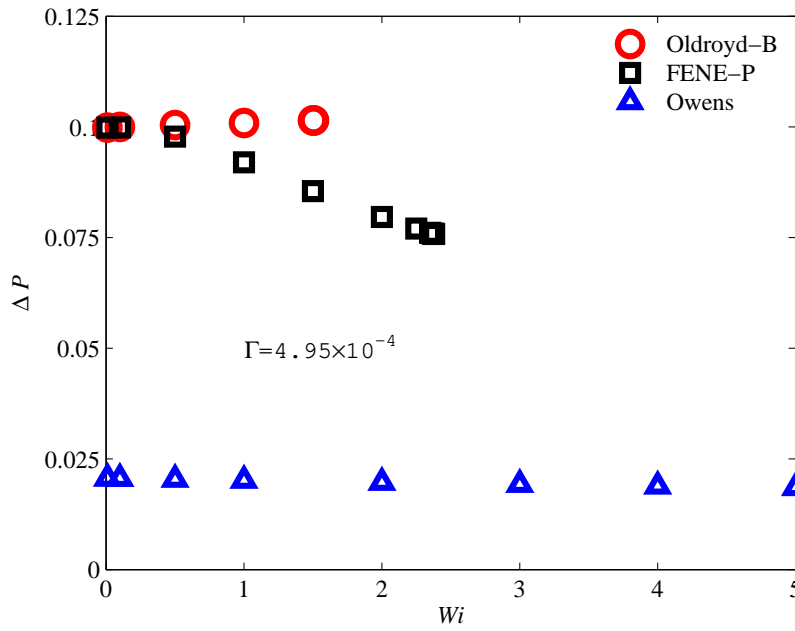
A different perspective on fluid pressure in the channel is provided in figure 14, where the pressure drop ΔP in the channel between the entrance and exit to the region beneath the elastic solid, is displayed. As seen earlier in figures 7 (a)-(b), with increasing Γ , the interface shape for the Oldroyd-B and FENE-P fluids moves from being concave downwards to convex upwards. Figure 14 (a) shows that this is accompanied by an increase in ΔP . Interestingly, the rate of change of ΔP with Γ has a point of inflection around $\Gamma \sim 3 \times 10^{-4}$, which is approximately the value at which the elastic solid becomes horizontal (see figures 7 (a)-(b), and inset to figure 14 (a)).

A striking manifestation of differences in the prediction of a macroscopic property, because of differences in fluid rheology, is displayed in figure 14 (b), where the dependence of pressure drop ΔP on Weissenberg number Wi is plotted. The Owens model fluid has a nearly constant pressure drop because the fluid has undergone significant shear thinning, and has an almost constant viscosity under the deformable elastic solid for all values of Wi . For the Oldroyd-B model on the other hand, which is a constant viscosity fluid, there appears to be a very slight increase in ΔP . Clearly, the decrease in pressure at the downstream end of the channel, is more than made up with the increase at the upstream end. For the FENE-P fluid, the increasing shear thinning with increasing Wi is reflected in figure 14 (b) with the observed decrease in ΔP .

Figure 15 explores the dependence of the axial component of the conformation tensor M_{xx} , along the flexible wall, on Γ and Wi . Figures 15 (a)-(c) show that an increase in Γ leads to a decrease in the degree of stretching experienced by the micro-structural elements, and that the value of M_{xx} in the Owens model is much less sensitive to the value of Γ compared to the Oldroyd-B and FENE-P fluids. For the latter two fluids, for values of $\Gamma \lesssim 3 \times 10^{-4}$, the elastic solid is concave



(a)



(b)

Figure 14: Dependence of pressure drop ΔP in the channel for the Oldroyd-B, FENE-P and Owens models on (a) Γ at a fixed value of $Wi=0.1$ and (b) Wi at $\Gamma = 4.95 \times 10^{-4}$. Note that for a Newtonian fluid, $\Delta P = 0.1$ in (b) micro-structural. The curves terminate at the limiting Weissenberg number for each model.

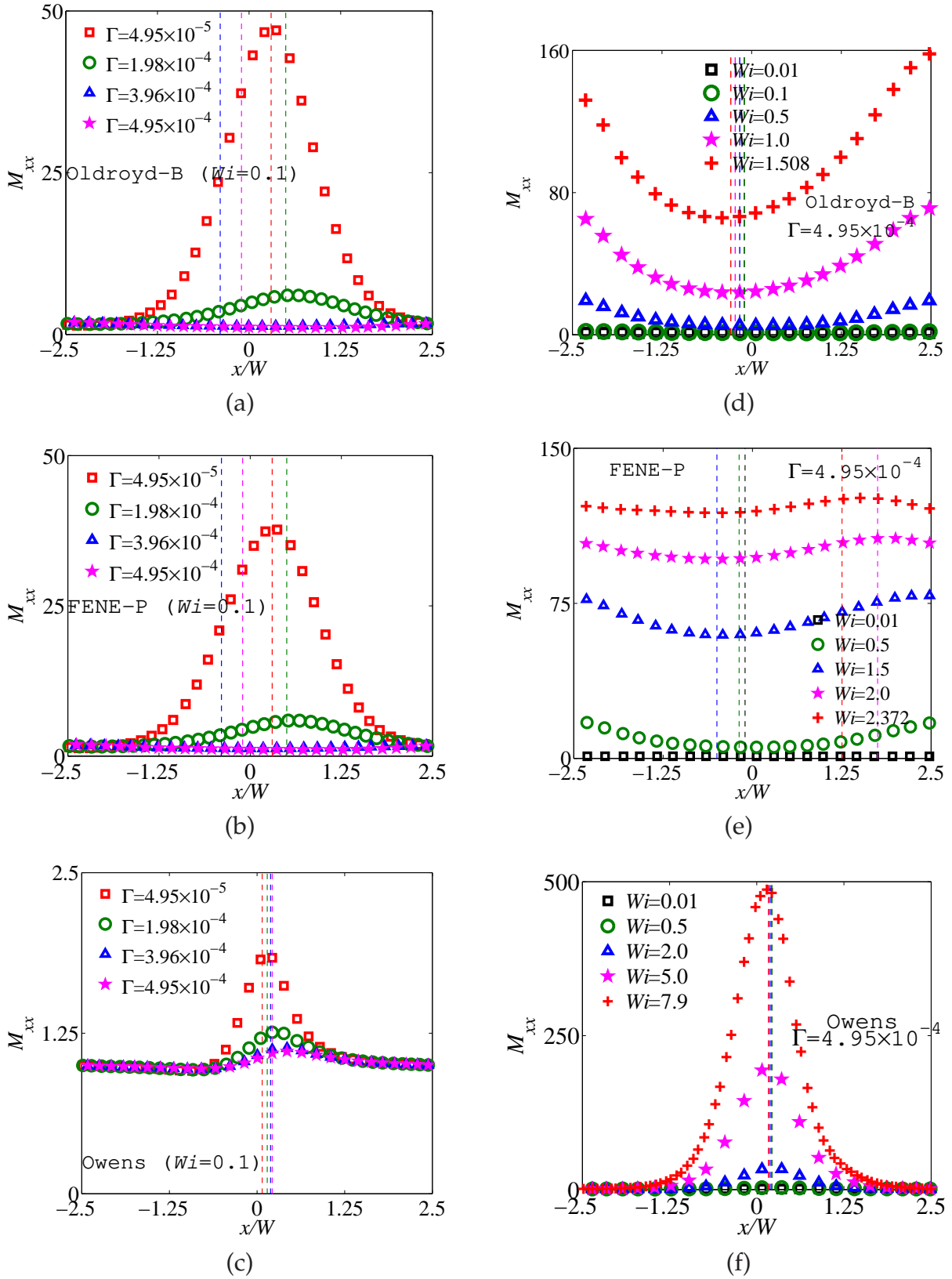


Figure 15: Dependence of the axial component of the conformation tensor M_{xx} on Γ , for (a) Oldroyd-B, (b) FENE-P, and (c) Owens models, at $Wi = 0.1$, and dependence of M_{xx} on Wi , for (d) Oldroyd-B, (e) FENE-P, and (f) Owens models, at $\Gamma = 4.95 \times 10^{-4}$.

downwards. As a result, the M_{xx} profile has a maximum at the location in the channel where the gap is narrowest. As the elastic solid moves out of the channel, there is a significant relaxation in the degree to which the micro-structural elements are stretched.

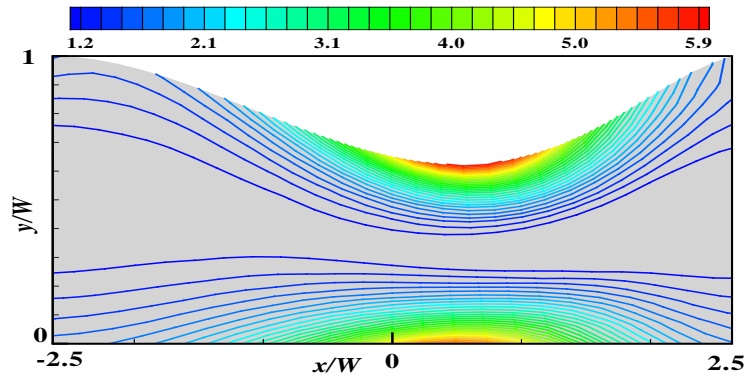
The correlation between interface shape and M_{xx} profile is more strikingly revealed in figures 15 (d)-(e), where the dependence of M_{xx} on Wi is explored at a constant value $\Gamma = 4.95 \times 10^{-4}$. Since the interface always bulges outwards for the Oldroyd-B and FENE-P fluids at this value of Γ , the highest stretch occurs at the *inlet* and *outlet* to the deformable region, in contrast to the situation for the Owens model, where the elastic solid is always concave downwards, and consequently, the maximum stretch is always at the location of the narrowest gap. At high values of Wi , the shear thinning experienced by the FENE-P fluid appears to lead to a more uniform stretching along the length of the channel. In all cases, however, as might be anticipated, an increase in Wi leads to an increase in stretching.

Figures 16 (a)-(c) show the contour plots of the mean streamwise molecular stretch M_{xx} for the Oldroyd-B, FENE-P and Owens models, at $\Gamma = 1.98 \times 10^{-4}$ and $Wi = 0.1$. As can be seen from figures 15 (a)-(c), these parameter values correspond to the situation where the elastic wall lies within the channel for all the fluids, and the values of M_{xx} for the Oldroyd-B and FENE-P models are close to each other along the entire length of the channel. Further, for all the models, the largest value of M_{xx} occurs below the collapsible wall at the minimum gap location. All these observations are clearly reflected in figures 16 (a)-(c), both in the shape of the interface and in the values of M_{xx} corresponding to the various contour lines.

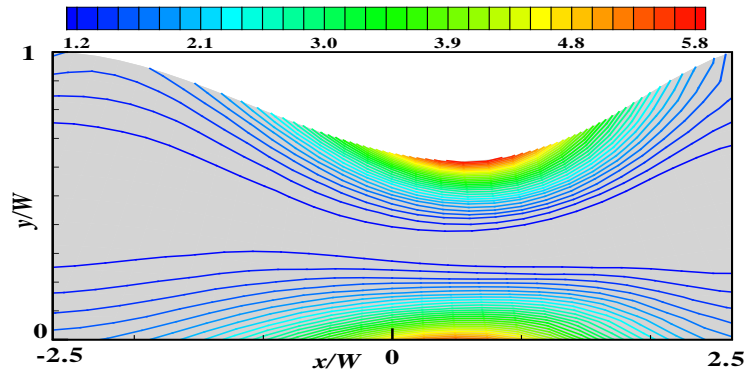
Finally, the dependence of the total shear stress on the elastic solid, $\tau_t^s + \tau_t^p$, on the parameters Γ and Wi , is examined in figure 17 for the three viscoelastic fluids. Once again, there is close parallel between the shape of the fluid-solid interface and the shear stress on the wall. Indeed, the shear stress profiles are either concave downwards or convex upwards in complete synchrony with the interface shape. In contrast to the zero-thickness membrane model, where the shear stress on the membrane has no influence on membrane shape because of the use of a boundary condition that only accounts for the influence of the normal stress, in the present model, both the pressure and the shear stress are responsible for the membrane shape. As a result, a much greater variety of interface shapes is observed for a finite thickness elastic solid.

4. Conclusions

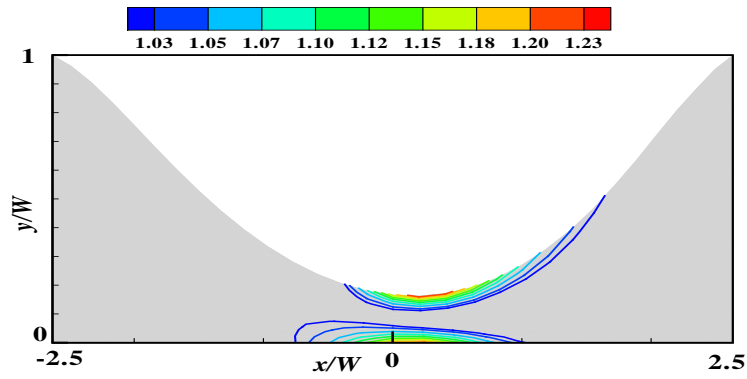
We have introduced a new geometry, whose central feature is the existence of fluid-structure interaction, into the lexicon of standard benchmark non-Newtonian flow computations. The role that the presence of a deformable membrane plays in the development of a complex flow field in the channel has been examined, and the relationship of the upper limit to the Weissenberg number to molecular conformations at various locations in the flow domain, has been delineated. The shape of the membrane as a function of a membrane elasticity parameter Γ , and of the Weissenberg number Wi has been studied, and the change in shape has been used as an indication of the extent of fluid-structure interaction. The nature of the coupling between macroscopic observables such as velocity, stress and conformation fields, and various rheological features of the three viscoelastic fluid models



(a)



(b)



(c)

Figure 16: Contours of M_{xx} in the flow domain for the Oldroyd-B, FENE-P and Owens models at $\Gamma = 1.98 \times 10^{-4}$, $P_e = 0.04$, $t = 0.4W$ and $Wi = 0.1$.

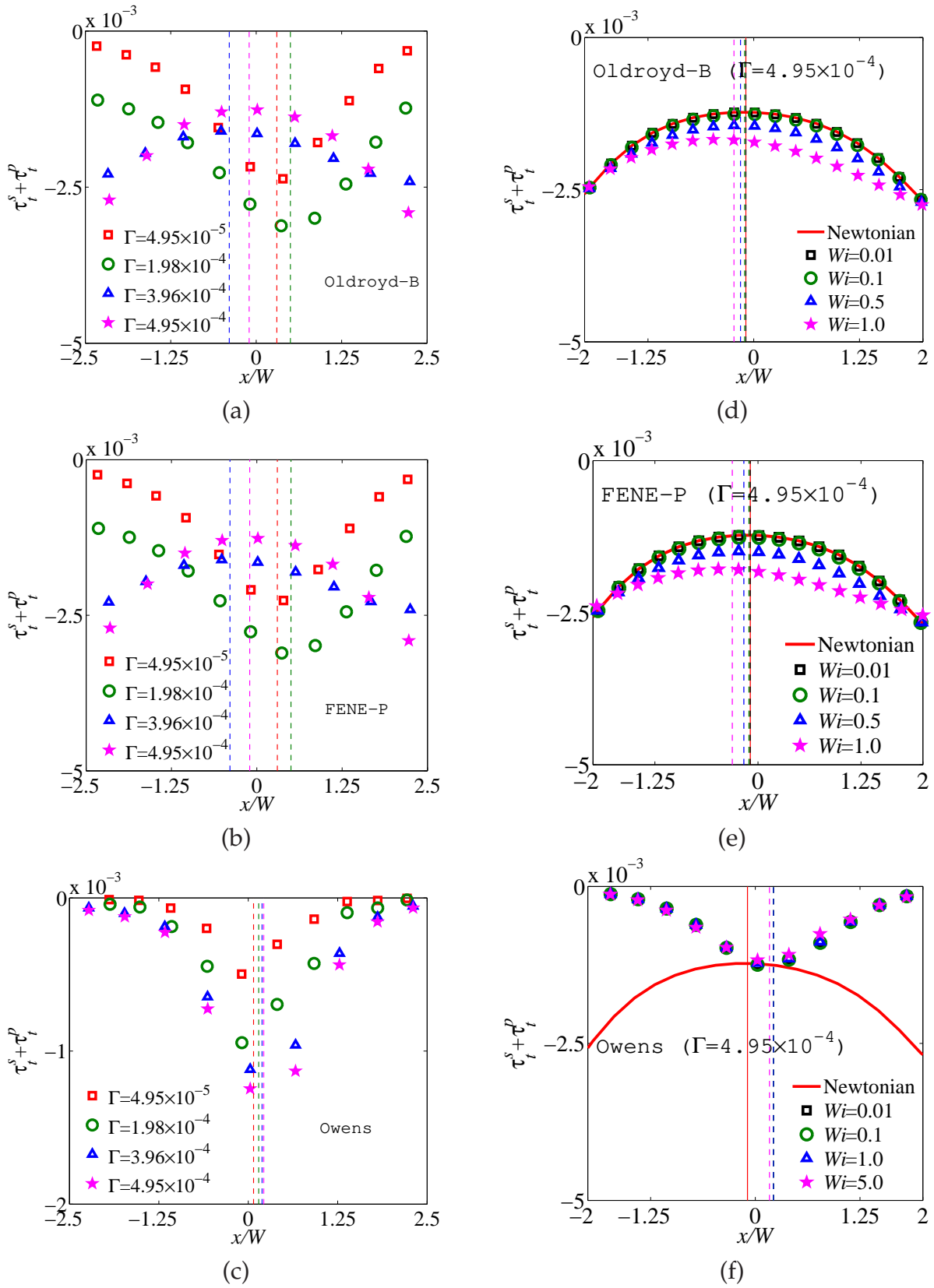


Figure 17: Dependence of the tangential component of stress $\tau_t^s + \tau_t^p$ on Γ , for (a) Oldroyd-B, (b) FENE-P, and (c) Owens models, at $Wi = 0.1$, and dependence of $\tau_t^s + \tau_t^p$ on Wi , for (d) Oldroyd-B, (e) FENE-P, and (f) Owens models, at $\Gamma = 4.95 \times 10^{-4}$.

used in this study, has been explored in some detail.

There are many aspects of viscoelastic flows in two dimensional collapsible channels that remain to be studied. (i) The use of a constitutive model that accounts for thixotropy is an important feature, since the aggregation of blood cells in regions of low shear rate can lead to rheological properties that depend locally on micro-structural dynamics. Owens model in its most general form does account for thixotropy [7], and as mentioned earlier, Iolov et al. [28] have recently developed a finite element method for solving the Owens model in its complete generality. (ii) Even though there exists an upper limit to the Weissenberg number at which computations fail for each mesh, we have not encountered, in our admittedly limited simulations, a situation where this upper limit has not changed in spite of mesh refinement. It would be interesting to see if the use of a log-conformation tensor formalism leads to much higher upper limits to the Weissenberg number for all the models. (iii) The multiple modes of instabilities that arise for flow in collapsible channels, and the rich behaviour that occurs in unsteady flows, has been extensively investigated for Newtonian fluids. We hope that the present work provides a starting point for similar studies in the context of viscoelastic fluids.

5. Acknowledgments

We thank Matteo Pasquali and Marcio Carvalho for providing us with their finite element code for simulating coating flows, which we have modified and adapted to this work. This work was supported by an award under the Merit Allocation Scheme on the NCI National Facility at the Australian National University (ANU). The authors also would like to thank the VPAC (Australia), and SUNGRID (Monash University, Australia) for the allocation of computing time on their supercomputing facilities.

Bibliography

- [1] J. B. Grotberg, O. E. Jensen, Biofluid mechanics in flexible tubes, *Annu. Rev. Fluid Mech.* 36 (2004) 121–147.
- [2] C. A. Taylor, M. T. Draney, Experimental and computational methods in cardiovascular fluid mechanics, *Annu. Rev. Fluid Mech.* 36 (2004) 197–231.
- [3] G. P. Galdi, R. Rannacher, A. M. Robertson, S. Turek, *Hemodynamical Flows: Modeling, Analysis and Simulation (Oberwolfach Seminars)*, Birkhauser, 2008.
- [4] A. Sequeira, J. Janela, An overview of some mathematical models of blood rheology, in: *A portrait of state-of-the-art research at the Technical University of Lisbon*, Springer, Netherlands, 65–87, 2007.
- [5] V. Cristini, G. S. Kassab, Computer modeling of red blood cell rheology in the microcirculation: A brief overview, *Ann. Biomed. Eng.* 33 (2005) 1724–1727.
- [6] O. K. Baskurt, H. J. Meiselman, Blood rheology and hemodynamics, *Semin. Thromb. Hemost.* 29 (2003) 435–450.

- [7] R. G. Owens, A new microstructure-based constitutive model for human blood, *J. Non-Newton. Fluid Mech.* 140 (2006) 57–70.
- [8] P. Kalita, R. Schaefer, Mechanical models of artery walls, *Arch. Comput. Method Eng.* 15 (2008) 1–36.
- [9] C. D. Bertram, Unstable equilibrium behaviour in collapsible tubes, *J. Biomech.* 19 (1986) 61–69.
- [10] C. D. Bertram, C. J. Raymond, T. J. Pedley, Mapping of instabilities during flow through collapsed tubes of differing length, *J. Fluids. Struct.* 4 (1990) 125–153.
- [11] A. I. Katz, Y. Chen, A. Moreno, Flow through a collapsible tube, *Biophys. J.* 9 (1969) 1261–1279.
- [12] A. H. Shapiro, Steady flow in collapsible tubes., *J. Biomech. Eng.-Trans. ASME* 99 (1977) 126–147.
- [13] O. Jensen, Instabilities of flow in a collapsed tube, *J. Fluid Mech.* 220 (1990) 623–659.
- [14] Z. X. Cai, X. Y. Luo, A fluid-beam model for flow in a collapsible channel, *J. Fluids. Struct.* 17 (2003) 125–146.
- [15] X. Y. Luo, B. Calderhead, H. F. Liu, W. G. Li, On the initial configurations of collapsible tube flow, *Comput. Struct.* 85 (2007) 977–987.
- [16] H. F. Liu, X. Y. Luo, Z. X. Cai, T. J. Pedley, Sensitivity of unsteady collapsible channel flows to modelling assumptions, *Commun. Numer. Meth. Engng* 25 (2009) 483–504.
- [17] O. E. Jensen, M. Heil, High-frequency self-excited oscillations in a collapsible-channel flow, *J. Fluid Mech.* 481 (2003) 235–268.
- [18] X. Xie, M. Pasquali, Computing 3D free surface viscoelastic flows, in: A. Mammoli, C. A. Brebbia (Eds.), *Moving Boundaries VII: Computational Modelling of Free and Moving Boundary Problems*, WIT press, Southampton, UK, 225–234, 2003.
- [19] X. Xie, *Modeling Viscoelastic Free Surface and Interfacial Flows, with Applications to the Deformation of Droplets and Blood Cells*, Ph.D. thesis, Rice University, Houston, TX, 2006.
- [20] A. L. Hazel, M. Heil, Steady finite-Reynolds-number flows in three-dimensional collapsible tubes, *J. Fluid Mech.* 486 (2003) 79–103.
- [21] A. Marzo, X. Luo, C. Bertram, Three-dimensional collapse and steady flow in thick-walled flexible tubes, *J. Fluids. Struct.* 20 (2005) 817–835.
- [22] D. Chakraborty, M. Bajaj, L. Yeo, J. Friend, M. Pasquali, J. R. Prakash, Viscoelastic flow in a two-dimensional collapsible channel, *J. Non-Newton. Fluid Mech.* 165 (2010) 1204–1218.

- [23] X. Y. Luo, T. J. Pedley, A numerical simulation of steady flow in a 2-D collapsible channel, *J. Fluids. Struct.* 9 (1995) 149–174.
- [24] D. Chakraborty, J. R. Prakash, Influence of Shear Thinning on Viscoelastic Fluid–Structure Interaction in a Two-Dimensional Collapsible Channel, *Ind. Eng. Chem. Res.* 50 (2011) 13161–13168.
- [25] D. Chakraborty, J. R. Prakash, J. Friend, L. Yeo, Fluid-structure interaction in deformable microchannels, *Phys. Fluids* 24 (2012) 102002.
- [26] M. S. Carvalho, L. E. Scriven, Flows in forward deformable roll coating gaps: Comparison between spring and plane strain models of roll cover, *J. Comput. Phys.* 138 (1997) 449–479.
- [27] M. Pasquali, L. E. Scriven, Theoretical modelling of microstructured liquids: A simple thermodynamic approach, *J. Non-Newton. Fluid Mech.* 120 (2004) 101–135.
- [28] A. Iolov, A. S. Kane, Y. Bourgault, R. G. Owens, A. Fortin, A finite element method for a microstructure-based model of blood, *Int. J. Numer. Meth. Biomed. Engng.* 27 (2011) 1321–1349.
- [29] J. Fang, R. G. Owens, Numerical simulations of pulsatile blood flow using a new constitutive model, *Biorheology* 43 (2006) 637–660.
- [30] D. Chakraborty, *Viscoelastic Flow in a Collapsible Channel*, Ph.D. thesis, Monash University, Clayton, Australia, 2011.
- [31] K. N. Christodoulou, L. E. Scriven, Discretization of free surface flows and other moving boundary problems, *J. Comput. Phys.* 99 (1992) 39–55.
- [32] J. M. de Santos, *Two-phase Cocurrent Downflow through Constricted Passages*, Ph.D. thesis, University of Minnesota, Minneapolis, MN. (Available from UMI, Ann Arbor, MI, order number 9119386), 1991.
- [33] D. F. Benjamin, *Roll Coating Flows and Multiple Roll Systems*, Ph.D. thesis, University of Minnesota, Minneapolis, MN. (Available from UMI, Ann Arbor, MI, order number 9512679), 1994.
- [34] M. Pasquali, L. E. Scriven, Free surface flows of polymer solutions with models based on the conformation tensor, *J. Non-Newton. Fluid Mech.* 108 (2002) 363–409.
- [35] X. Xie, M. Pasquali, A new convenient way of imposing open-flow boundary conditions in two and three-dimensional viscoelastic flows, *J. Non-Newton. Fluid Mech.* 122 (2004) 159–176.
- [36] R. Guénette, M. Fortin, A new mixed finite element method for computing viscoelastic flows, *J. Non-Newton. Fluid Mech.* 60 (1995) 27–52.
- [37] G. A. Zavallos, M. S. Carvalho, M. Pasquali, Forward roll coating flows of viscoelastic liquids, *J. Non-Newton. Fluid Mech.* 130 (2005) 96–109.

- [38] M. Bajaj, J. R. Prakash, M. Pasquali, A computational study of the effect of viscoelasticity on slot coating flow of dilute polymer solutions, *J. Non-Newton. Fluid Mech.* 149 (2008) 104–123.
- [39] S. Chien, Shear dependence of effective cell volume as a determinant of blood viscosity, *Science* 168 (1970) 977–979.
- [40] A. M. Robertson, A. Sequeira, M. V. Kameneva, Hemorheology, in: G. P. Galdi, R. Rannacher, A. M. Robertson, S. Turek (Eds.), *Hemodynamical Flows: Modeling, Analysis and Simulation (Oberwolfach Seminars)*, Birkhauser, 63–120, 2008.
- [41] X. Deng, R. Guidoin, Arteries, veins and lymphatic vessels, in: J. Black, G. Hastings (Eds.), *Handbook of Biomaterial Properties*, Chapman & Hall, London, 81–105, 1998.
- [42] H. D. Intengan, L. Y. Deng, J. S. Li, E. L. Schiffrin, Mechanics and Composition of Human Subcutaneous Resistance Arteries in Essential Hypertension, *Hypertension* 33 (1) (1999) 569–574.
- [43] X. Zhang, M. Fatemi, J. F. Greenleaf, Inverse method for estimating elastic modulus of arterial walls, *2004 SPIE Int. Symp. Medical Imaging* 5368 (2004) 226–235.
- [44] X. Zhang, J. F. Greenleaf, Generation of ring resonant mode for measuring artery elastic modulus, *Medical Imaging 2005, Proc. of SPIE* 5750 (2005) 236–243.
- [45] X. Zhang, J. F. Greenleaf, Noninvasive estimation of local elastic modulus of arteries with the ring resonance measurement, *IEEE Int. Ultrasonics Symp.*, October 3–6, Vancouver, Canada (2006) 1161–1164.
- [46] X. Zhang, J. F. Greenleaf, Estimation of complex arterial elastic modulus from ring resonance excited by ultrasound radiation force, *Ultrasonics* 44 (Suppl. 1) (2006) e169–e172.
- [47] J. Zanden, M. Hulsen, Mathematical and physical requirements for successful computations with viscoelastic fluid models, *J. Non-Newton. Fluid Mech.* 29 (1988) 93–117.
- [48] P. Singh, L. Leal, Finite-element simulation of the start-up problem for a viscoelastic fluid in an eccentric rotating cylinder geometry using a third-order upwind scheme, *Theor. Comput. Fluid Dyn.* 5 (1993) 107–137.
- [49] N. A. Patankar, P. Y. Huang, D. D. Joseph, H. H. Hu, Normal stresses on the surface of a rigid body in an Oldroyd-B fluid, *ASME J. Fluids Eng.* 124 (2002) 279–290.